Electric Field Response of Strained $BiFeO_3$ and $BaTiO_3/CaTiO_3$ Superlattices

By

Margaret P. Cosgriff

A dissertation submitted in partial fulfillment of the requirements for the

degree of

Doctor of Philosophy

(Physics)

at the

UNIVERSITY OF WISCONSIN-MADISON

2015

Date of final oral examination: January 6, 2015

The dissertation is approved by the following members of the Final Oral Committee:
Professor Susan Coppersmith, Physics
Professor Mark Eriksson, Physics
Professor Paul Evans, Materials Science and Engineering
Professor Franz Himpsel, Physics
Professor Mark Rzchowski, Physics

Abstract

Complex oxide materials can be driven into transient structural configurations using applied electric fields. Structural changes significantly impact the functional properties of these materials, including their piezoelectricity. Piezoelectric materials grown as heteroepitaxial thin films have therefore attracted much attention because the choice of substrate crystal structure significantly affects the film structure, particularly the in-plane lattice parameter. We report the development of methods to study the structure of complex oxide thin-film materials, strained $BiFeO_3$ films and $BaTiO_3/CaTiO_3$ superlattice films, and the application of these tools to probe the response of the crystal structure to applied electric fields. The structural studies use laboratory and synchrotron-based x-ray diffraction to probe the static structure of these layers, and include time-resolved synchrotron x-ray microdiffraction to characterize the structural response to applied fields.

The study of superlattice thin films composed of alternating layers of $BaTiO_3$ and $CaTiO_3$ focuses on rotations of the oxygen octahedral building blocks of the perovskite structure. By examining the characteristic x-ray reflections produced by the octahedral rotations, we find these rotations are present in $n(BaTiO_3)/(6-n)(CaTiO_3)$ superlattices for $n = (2,3,4)$. More intense reflections are produced by superlattice compositions with more consecutive $CaTiO_3$ layers. The pattern of octahedral rotations present in the $2(BaTiO_3)/4(CaTiO_3)$ composition is only coherent over one superlattice unit in the out-of-plane direction, indicating that the octahedral rotations between $BaTiO_3$ layers are suppressed. We also find the response of these rotations to applied electric fields is far

ii

larger for fields with durations of on the order of 1 ms than for pulse-durations on the order of hundreds of nanoseconds.

The study of strained $BiFeO_3$ thin films probes the electric-field driven structural phase transition from an initial state consisting of M and T_{tilt} phases, to the tetragonal-like T phase. The application of an electric field increased the fraction of the film in the T phase at the expense of the M and T_{tilt} phases. An additional fraction of the film is transformed to the T phase during the electric field pulse, reverting to the M phase when the field is removed. Different M phase populations respond differently to applied electric fields.

Table of Contents

Acknowledgements

I would like to thank our collaborators Dr. Ho Nyung Lee, Dr. Zuhuang Chen and Dr. Lang Chen's research group, who grew the samples we used. I am also grateful for the support of Dr. Apurva Mehta at SSRL and Dr. Hiroo Tajiri at SPring-8, who developed and maintained the facilities we used and taught me how to work with them. I am grateful for the efforts of Prof. Xifan Wu, whose DFT calculations were crucial during the beginning of the superlattice study. I would also like to thank Prof. Ji Young Jo for her help and advice, and Sung Su Lee and Hyeon Jun Lee for their help during experiments at SPring-8.

I would like to thank the members of our research group for all the assistance and support they provided. Dr. Rebecca Sichel showed me how to do x-ray diffraction when I was just starting in graduate school. Dr. Pice Chen was always eager to answer all of my questions, and was an extremely valuable person to be working with during experiments at light sources.

I would like to thank my advisor Prof. Paul Evans for giving me direction and encouragement, helping me get from vague notions to actual results. I would like to thank Renee Lefkow, who has helped me navigate the intricacies of graduation from prelim to thesis to defense.

Finally, I would like to thank my parents for their constant support and understanding during my time here, my brother Arthur for helping me stay grounded when things seemed overwhelming, and George for helping me through everything by going through it with me.

Chapter 1: Introduction

1.1 Perspective

The useful functional electronic and electromechanical properties of materials can be systematically controlled using small changes in composition or by varying externally applied fields including mechanical stresses. Small changes in the composition of ferroelectric oxides, for example, can be used to vary the piezoelectric and dielectric properties of those materials. Ferroelectric materials are often of interest due to their piezoelectric properties, which make them useful in a variety of devices as sensors and actuators.[1,2] In terms of the variation of the composition, the choice of the composition of an oxide that consists of a mixture between the compounds lead titanate ($PbTiO_3$) and lead zirconate ($PbZrO_3$) has a very large effect on piezoelectricity.[3] As we review in detail below, the phenomenon responsible for this large series of changes in the properties is the difference in structural symmetry between materials made from the pure components.[4] Varying the externally applied mechanical pressure at fixed composition

can have similar effects on the functional properties.[5] The applied pressure can yield phase transitions between crystallographic structures with different symmetries that are similar to the changes produced by changes in composition.[5] Applied electric fields can produce similar changes in the structure, and these can either disappear or persist after the field is removed, depending on the material. A key aspect of the previous work in this field has been that the external parameters have been either very slowly varied (e.g. as in the case of applied pressures) or completely static. This thesis describes a series of experiments designed to probe the dynamics of the relationship between applied electric fields and the structural changes such as those responsible for the large effects observed near phase transitions.

The work in this thesis illustrates two sets of effects of applied electric fields on the structure of thin film ferroelectric materials. In a first series of experiments, conducted using superlattices consisting of alternating layers of barium titanate ($BaTiO_3$) and calcium titanate ($CaTiO_3$) we show that electric fields can induce subtle structural changes and that the way in which these changes occur can have important effects on other functional properties. Our work in these $BaTiO_3$/$CaTiO_3$ superlattices demonstrates that there is a link between the static structure of the superlattice, the distortion of the static structure induced by an applied electric field, and the dynamics of structural changes.

A second series of experiments is based on the concept that materials can exhibit extremely large responses to external fields (i.e. the electric field in our case) if the system is already at a composition or mechanical stress that places it near the boundary between two phases. The concept of using such phase boundaries is extremely general.

Here we examine in particular the expansion of the lattice and the transformation between structural phases in bismuth ferrite ($BiFeO_3$ or BFO). The transformation we observe in BFO is similar to field-induced phase transitions leading to extremely large piezoelectric response in ferroelectric oxides such as the $PbTiO_3$-$PbZrO_3$ system discussed above or a similar effect in the $PbMgO_3$/$PbNbO_3$-$PbTiO_3$ (PMN-PT) system.[3,6] It is also interesting to note that large responses to applied fields also occur in a number of other systems, including in materials that are not ferroelectric. The dielectric constants, magnetic susceptibility, and magnetoresistance can also exhibit large responses at phase transitions in a wide range of materials.[7,8] A common characteristic of such materials is that the high response is achieved under conditions near those in which multiple phases with distinct properties coexist.[9] The work presented in this thesis probes the transformation between structural states in BFO and for the first time shows that the dynamics of such a transition can be extremely fast, limited in our case only by the design of the electrical devices in which they were probed.

This chapter introduces the fundamental concepts that are needed to study electric-field induced structural changes in complex oxide thin films. The key pieces of this background are (i) fundamental concepts associated with the synthesis of thin-film electronic materials and (ii) recent advances in x-ray scattering techniques using synchrotron-radiation light sources that permit studies of these materials in large transient applied electric fields.

1.2 Structure and Design of Oxide Thin Films and Superlattices

There has been a rapid and dramatic series of developments in the synthesis of oxide materials using thin film growth techniques.[10] Crystalline oxide thin films build on the fundamental concept of epitaxy, which is the idea that atoms deposited onto single crystal substrates can, under the correct conditions, propagate the crystalline structure of the substrate into the growing layer. Epitaxial thin film layers are deposited using precise control of the flux of atoms to the surface and thin films can thus be grown with abrupt and arbitrary changes in composition, permitting the development of precise sequences of atomic-scale layers. The flux of atoms to the surface can be provided using precursor gasses, thermal evaporation of elemental sources, by sputtering from targets with similar composition to the growing film, or by the laser ablation of a target.[10]

The experiments described in this thesis rely on epitaxial synthesis, as applied in the research groups of my collaborators, to create thin film materials with properties that are distinct from even bulk materials of the same composition. The two key physical effects in epitaxial growth that are employed in the creation of these thin films are the introduction of larger interfacial stresses during the growth of strained heteroepitaxial layers and the creation of layered superlattice materials consisting of alternating layers of different composition.

1.2.a Strained heteroepitaxial films

Growing a thin film of one material on a substrate crystal of another material can modify the crystallographic structure of the growing thin film. The simplest cases occur when the chemical composition and crystallographic of the thin film and substrate are

similar. This is often the case in oxide materials that have a crystal structure based on a distortion of the simple-cubic perovskite structure. Here the growing material often adopts an in-plane lattice parameter that matches the lattice parameter of the substrate, rather than the lattice parameter exhibited by the thin film material in its bulk form. The difference in lattice parameters is quantified using the biaxial strain, defined as $(a - a_0)/a_0$, where a and a_0 are the cubic (or pseudocubic) lattice parameters of the thin film and equilibrium bulk forms, respectively. The materials we describe in this thesis have structures that are sufficiently close to cubic symmetry that we can treat their structures as cubic. With this pseudocubic approximation the strain throughout the theses can be determined using the simple cubic definition of the biaxial strain.

The magnitude of the strain imposed by epitaxial growth can be chosen by selecting a substrate with an in-plane crystal lattice parameter that is different from the bulk form of the growing film. The substrate can have either larger or smaller lattice parameter than a_0, imposing tensile or compressive stresses on the growing film and resulting in compressive or tensile biaxial stress in the completed material once it is returned to room temperature following the growth process. A further complication in systems that do not exhibit cubic symmetry is that the symmetry of the thin film and substrate can be different. The angle between the primitive vectors of the substrate can also differ from the film material, for example. The basic concepts of epitaxy have been exploited extensively in creating the BFO thin films introduced below in section 1.2.c and discussed extensively in Chapter 4.

1.2.b Superlattices

 The versatility of epitaxial growth techniques allows the composition of growing thin films to be changed with sufficient precision that interfaces between layers of different composition can be atomically sharp. Thin-film superlattices, as illustrated in Figure 1.1, consist of a stack of many copies of a repeating unit consisting of crystalline sub-layers of more than one material. The compositions of these sub-layers are termed A and B in the diagram of a two-component superlattice in Figure 1.1. More elaborate structures can consist of three or more compositionally distinct layers. These superlattices can have properties that are not intuitively derived from the properties of the component materials.

 Chapter 3 of this thesis focuses on superlattices consisting of alternating ferroelectric and dielectric components. In ferroelectric/dielectric (FE/DE) superlattice films, the polarization of the ferroelectric layers can extend partially into or completely through the dielectric component, depending on the thickness, dielectric permittivity, and
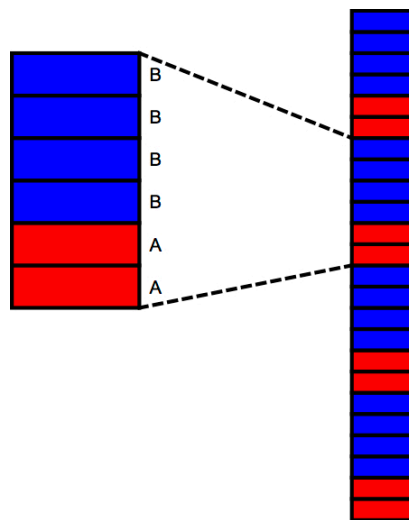
Figure 1.1 Two-component thin film superlattice with a repeating unit consisting of two unit cells of a crystal with composition A and 4 unit cells of composition B.

structure of the dielectric layers in the superlattice.[11] The development of ferroelectric

remnant polarization in the dielectric layers in these films can cause the material to

potentially exhibit greater ferroelectric remnant polarization than the ferroelectric

component in bulk.[12] One potential practical impact of ferroelectric/dielectric

superlattices is thus in the design of novel ferroelectric materials that cannot be created

by bulk synthesis techniques.

Studies of the piezoelectric properties of ferroelectric/dielectric superlattices show,

however, that their piezoelectricity can also differ from the piezoelectric properties of the

ferroelectric component in its bulk. The piezoelectric response of a superlattice

composed of a pattern of two layers of ferroelectric $BaTiO_3$ (BFO) and four layers of

dielectric $CaTiO_3$ (CTO), for example, is equivalent to what is expected from a uniform

ferroelectric in applied electric fields with relatively long millisecond durations.[13] The

magnitude of the piezoelectric strain generated during shorter nanosecond-duration

electric field pulses is far smaller, suggesting that structural phenomena more

complicated than the development of polarization in the dielectric component are

important.[14] The relationship between the presence of CTO layers in the film and the

film's delayed piezoelectric response is explored in Chapter 3.

1.2.c BiFeO$_3$

Multiferroic magnetic materials possess both ferroelectric and magnetic order, and

can exhibit a coupling between magnetic and electronic properties.[15] $BiFeO_3$ (BFO) has

the unusual property of being multiferroic at room temperature, possessing both

antiferromagnetic order of its magnetic moments and large ferroelectric remnant

polarization.[16] The unusual combination of magnetic and ferroelectric polarizations, combined with relatively straightforward epitaxial synthesis have made BFO the subject of extensive study regarding its magnetic and electrical properties and its crystal structure.[17-19]

The crystallographic structure of BFO depends on the boundary conditions imposed by epitaxial growth. Strained BFO films have room-temperature crystallographic symmetries that depend on both the degree of biaxial strain imposed by the substrate and on the thickness of the film.[20] The effect of the film thickness arises largely because the degree of epitaxial strain is reduced via the formation of crystallographic defects or ferroelectric polarization domains. Films under little or no strain, with biaxial strains with magnitude less than 1%, have a nearly-rhombohedral monoclinic crystal structure that is ferroelectric,[21] similar to the rhombohedral crystal structure of bulk BFO. Under large compressive strain (-4.5%), thin BFO films (<40 nm) take on a nearly tetragonal monoclinic structure that is also ferroelectric.[21] Under tensile strain, BFO develops domains with orthorhombic crystal structure.[22] In compressively strained BFO thicker than 40 nm, additional triclinic phases can also be present.[20]

The subtle differences between the crystallographic structures of the different phases of BFO have important consequences for its electronic and piezoelectric properties. The most important difference is that the ferroelectric remnant polarization in BFO points along different directions in the different structural phases. These differences are discussed in detail in Chapter 4.

As a result of the differences in the direction of the remnant polarization vectors in its different phases, BFO films can be driven between phases by the application of an

electric field. The boundary between phases occurs at a series of values of the magnitude of the applied electric field that depends on the magnitude of the compressive strain imposed during epitaxial growth. For small compressive strains the films exhibit dielectric breakdown before the electric field is sufficiently large to induce the structural phase transitions.[23] At compressive strains with magnitudes of 4 to 4.5%, however, the BFO film is near a strain-induced morphotropic phase boundary between the mixed and nearly tetragonal phases.[24] This effect of the biaxial strain in BFO is similar to the effect of hydrostatic pressure in bulk ferroelectrics.[5] Previous studies of the electric-field-induced transition between structural phases have found that the BFO layer can remain in either of these phases indefinitely once switched.[19]

An important consequence of the electric-field-induced phase transition arises from the difference in the lattice parameters of the tetragonal and mixed phases of BFO. The tetragonal phase has a lattice parameter that is approximately 5% larger along the direction normal to the surface of the thin film. The transition between the phases thus results in a large displacement of the surface of the BFO thin film, with a magnitude of the displacement that can be as much as the 5% difference in lattice parameters.[9] The large surface displacement arising from the phase transition is effectively an extremely large enhancement of the piezoelectric response of BFO, which makes fundamental study of the mechanism and dynamics of the transition particularly important.

1.3 Experimental Techniques

Our primary tool for observing the structure of BFO thin films and BTO/CTO superlattices was x-ray diffraction. The sophisticated measurements of the changes in the

structure of these thin films induced by applied electric fields required the use of synchrotron x-ray radiation from a storage ring facility. The measurements that are described in this thesis were performed using two different synchrotron radiation facilities. The steady-state structure of the BTO/CTO superlattices was characterized using the facilities at the Stanford Synchrotron Radiation Lightsource at SLAC National Accelerator Laboratory, Menlo Park, CA. The *in situ* studies of the structural response of both the BFO and BTO/CTO samples were performed using the SPring-8 light source at Hyogo, Japan. The key difference between the two sources is in the brilliance of the x-ray beams that are available for experiments. The higher brilliance of the SPring-8 sources permitted the use of the focusing optics necessary to study small thin-film capacitor samples and provided sufficient intensity to allow time-resolved measurements. Preliminary characterizations of the film structures were performed using a laboratory x-ray diffractometer located in the Engineering Research Building on the UW-Madison campus.

The experimental requirements of the x-ray diffraction experiment can be made clear by examining the design of the experiment studying the response of BTO/CTO superlattices to applied electric fields. In the case of the BTO/CTO system, the x-ray reflections that are important to the structural response arise from displacements of oxygen atoms due to the rotation of the oxygen octahedra structural building block of the perovskite structure. Due to the small magnitude of these displacements (0.3 Å for a 10° rotation), and the relatively low atomic number of oxygen (8) compared to the other elements in the superlattice (20 for calcium, 56 for barium), these reflections are two orders of magnitude weaker than the Bragg reflections caused by the averaged perovskite

structure of the superlattice. The reflections are weak enough, in fact, that it is quite

difficult to observe them with a laboratory diffractometer, where at maximum power they

have intensities of approximately 10 counts/s.

Observing the dynamics of the responses of the B2C4 superlattice and BFO films

to applied electric fields posed the additional challenge of using x-ray diffraction to make

time-resolved measurements. Making these measurements effectively requires that the x-

ray intensity be increased because the measurement must be repeated at a large number of

time points corresponding to different magnitudes of the applied electric field. In

addition, the time-resolved studies often require repetition rates of the applied electric

field that are far lower than the total repetition rate of x-ray pulses from the synchrotron

light source. The typical arrival rate of pulses from the light sources, corresponding to

the reciprocal of the time interval between pulses shown in Figure 1.2, below, is on the

order of 5 MHz. The repetition rate of electric field pulses is limited to approximately 20

kHz to avoid heating the electrodes of the sample. The net effect of the combination of

the need to repeat the experiment at many time points and to discard diffraction

information from pulses with no electric field was that the acquisition of time-resolved x-

ray data in applied fields required approximately two orders of magnitude longer than the

acquisition of the initial zero-field data.

The x-rays produced by synchrotron light sources arrive at the sample in short-

duration (less than 100 ps at Spring-8) pulses, with long (24 to 1500 ns, depending on

operating mode) gaps between pulses. The pulses are an inherent result of the way that

synchrotron light sources operate, each pulse is produced by an electron bunch passing
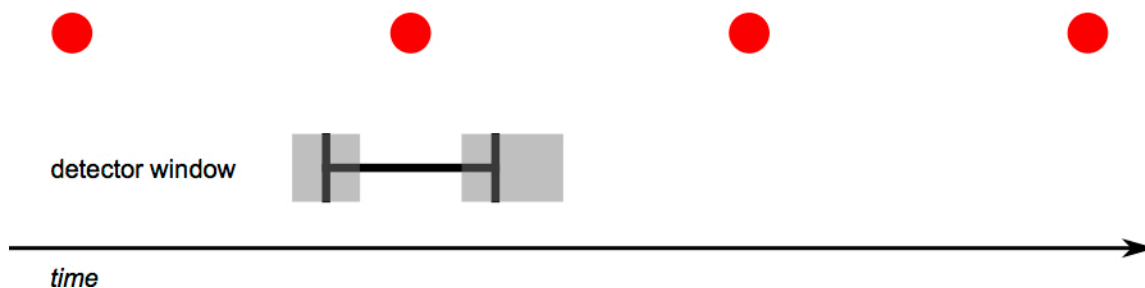
Figure 1.2 Synchronization of the recording window of a detector and an x-ray pulse. The uncertainty in the times the detector starts and stops counting (indicated by the gray boxes), does not degrade the time resolution of the measurement.

through the magnetic field produced by an insertion device or bending magnet. This time-profile of the x-ray intensity is quite different than the continuous beam of x-rays produced by the rotating anode x-ray generator used in our lab diffractometer.

The time resolution of experiments conducted using a continuous x-ray beam, such as the beam produced by a laboratory x-ray diffractometer, is limited by the x-ray detector. The shortest interval that can be resolved depends on how well the detector can distinguish x-rays with arrival times separated by small time intervals. At synchrotron light sources, because the x-rays are produced in short pulses with long gaps between pulses, the time-resolution limitations of the detector are less important. The detector can be set to start recording in the time interval before a particular x-ray pulse, and stop recording in the interval following that pulse. The time resolution of measurements using pulsed sources is then limited only by the duration of the pulse. In practical experiments, however, a finite time is required to excite the sample, e.g. the time required develop the electric field across the film, set by the charging time constant of the thin-film capacitor. In the experiments reported in this thesis the time resolution is effectively set by the sample rather than by the x-ray source. The experimental arrangement for measurements with a pulsed x-ray source is shown schematically in Figure 1.2.

The time-resolution available at SPring-8 allowed us to make observations of short-lived non-equilibrium structural states. These observations were particularly useful in our study of BTO/CTO superlattices because they helped us to explain the unexpectedly small piezoelectric response at short timescales. Being able to make measurements on this time-scale also allowed us to observe the response of our films to higher electric fields than would otherwise have been possible without damaging the films, by enabling us to apply those fields for a sufficiently short period of time as to avoid causing damage while still having enough time to make the measurement.

Being able to make time-resolved x-ray diffraction measurements also allowed us to observe transitions between states, such as the transition between crystallographic phases undergone by a BFO film during the application of an electric field. Previous studies had observed this phase switching by comparing measurements made before and after applying an electric field. Observing the dynamics of the response of a strained BFO film to an applied electric field, however, in general requires making measurements while the field is being applied, and in particular at different times relative to the initial application of the field.

Chapter 2: Methods

2.1 Introduction

The key experimental methods of this thesis are thin-film x-ray diffraction techniques. These experiments used x-rays generated at two different types of sources. A diffractometer using x-rays generated by a rotating anode x-ray generator allowed us to make preliminary studies of the structure of the samples, letting us map out our regions of interest in reciprocal space before making more detailed studies with the synchrotron sources. The synchrotron x-ray sources provided the intensity required to make detailed measurements of structural features in the BTO/CTO system that produced weak x-ray reflections. In addition, the x-ray beams produced by synchrotron radiation sources allowed experiments to have the combination of spatial and temporal resolution required to measure the dynamic response of these films to applied electric fields. The techniques and procedures associated with the use of both of these types of x-rays sources are explained in detail in this chapter.

The experiments probing the structural response to applied electric fields required combining x-ray diffraction experiments with sample geometries and electronics that provided a precise sequence of voltage pulses. The electric fields were generated by applying a voltage across the thickness of a thin-film capacitor defined by the top and bottom of the thin-film sample. The voltage pulses were generated using a pulse generator, which was triggered at a set repetition rate and time controlled by a digital circuit that we termed the timing circuit. The pulse generator allowed us to control the magnitude and duration of the electric fields we applied, letting us probe the response on different time scales. The timing circuitry enabled us to synchronize our x-ray measurements to the arrival of an x-ray pulse from the synchrotron and the application of an electric pulse from the pulse generator. The timing circuit also provided the means to control the time at which the electric-field pulses arrive relative to the x-ray pulses from the synchrotron light source. By varying the delay between the arrival of the electric fields and the x-ray probe pulse we effectively measured the structural response at different times after the electric pulses were applied.

Figure 2.1 Schematic of the reciprocal space of a BaTiO$_3$/CaTiO$_3$ heteroepitaxial superlattice. X-ray reflections arising from the undistorted perovskite structure occur along the rods of intensity shown in black. A series of rods arising from the oxygen octahedral rotations are shown in red.

As described in detail in Chapter 3, the key features of the reciprocal space of the BTO/CTO superlattices were a series of weak x-ray reflections arising from the rotation of the oxygen octahedral building blocks of the perovskite structure. The reciprocal-space locations of these reflections are illustrated in Figure 2.1. We term the weak reflections arising from octahedral rotations half-order reflections because they appear at half-integer values of the diffraction indices H K and L associated with the nominal crystallographic unit cell. A systematic study of the half-order reflections allowed us to understand the relationship between the number of unit cells of BTO and CTO in each repeating unit of the superlattice and the rotation of the octahedra. Time-resolved diffraction studies of these weak reflections allowed us to understand how the rotation of the oxygen octahedra varied during the applied electric field.

The structure associated with the rotation of the oxygen octahedra within the perovskite structure is described in detail in Chapter 3. The key point with respect to the design of our experiments and experimental methods is that an estimate of the magnitude of the octahedral rotation could be obtained by observing the intensities of the half-order reflections that are present. Measuring the intensities accurately does not require spatial or temporal resolution, or precise angular resolution, and we thus made these measurements using the laboratory diffractometer. Using the laboratory diffractometer allowed us to take extra time and care finding and measuring these reflections, which was important given their low intensity.

Studies of the half-order reflections with higher angular resolution were designed to determine the characteristic coherence length of the octahedral rotation patterns. These measurements required greater intensity and angular resolution than were available at the

laboratory diffractometer. Using station 10-2 of the Stanford Synchrotron Radiation

Lightsource (SSRL) we measured the reciprocal-space widths of multiple half-order

reflections in all three reciprocal-space directions.

The measurements of the response to applied electric fields required that the x-ray

beam probe a region of 10 μm or less with excellent time resolution. For these

measurements we used beamline BL13XU at the SPring-8 light source. The key feature

of BL13XU was that its diffractometer was located at a large distance from an x-ray

source with very high brilliance, allowing the x-rays to be focused to a small spot on the

sample. The electron bunches in the SPring-8 synchrotron storage ring were also short

enough to provide the time resolution we wanted. We used this beamline to perform

electric field response measurements for both a BTO/CTO superlattice sample and the

BFO film sample.

2.2 Sample Synthesis

The thin film samples for this study were fabricated using precise epitaxial growth

techniques by the research groups of two collaborators. The BTO/CTO superlattices were

grown in the research group of Dr. Ho-Nyung Lee of Oak Ridge National Laboratory.

The BFO thin films were grown by the research group of Prof. Lang Chen at the National

University of Singapore.

In both cases, the thin films were grown in vacuum using pulsed laser deposition.

Pulsed laser deposition uses a short focused laser pulse to vaporize material from a target.

The material that is ejected from the target by each pulse forms a plume of plasma, which

then allows the material to collect on the surface of the film substrate. The process is

conducted in vacuum in order to minimize contamination and to facilitate transport of the ejected material to the substrate surface. The substrate is held at a temperature that can be varied to optimize film deposition. This process is repeated until the film reaches the desired thickness.[25] The laser can also alternate between multiple targets in the chamber. By switching between different target materials more complex films, such as superlattices, can be grown.[12]

For oxides such as the BTO/CTO superlattices and BFO thin film described in this thesis, the deposition in the vacuum chamber can result in the loss of oxygen during the transfer of material from the target to the thin film. In addition, elevated temperatures are required to provide sufficient mobility of the deposited atoms to allow the film to grow with a small number of crystallographic defects. These high temperatures can lead to the loss of oxygen from the thin film. For both of these reasons, the deposition is conducted in an oxygen environment at a relatively high pressure of a fraction of approximately 100 mTorr in order to ensure that the film is as completely oxidized as possible.

The BFO film was grown epitaxially on a (0 0 1) $LaAlO_3$ (LAO) substrate. For the purposes of this thesis, LAO can be pictured as approximately cubic with an in-plane lattice parameter of 3.79 Å.[24] The growth of BFO on the LAO substrate imposes a biaxial compressive strain of -4.4% on the BFO film. The BFO film was grown at a temperature of 700° C and a pressure of 100 mTorr. The total thickness of the BFO layer was 70 nm. A layer of $LaNiO_3$ was grown between the substrate and the BFO film to be used as a bottom electrode. The top electrodes were formed using an array of Au thin films with a diameter of 50 μm that were deposited in a square grid on the surface of the film. The Au electrodes with spaced on 200 μm centers.

The BTO/CTO superlattice samples were grown epitaxially on (0 0 1)-oriented

SrTiO$_3$ (STO) substrates. The biaxial strains imposed on the components of this system

are thus -2.2% for BTO and +1.1% for CTO. The superlattice films were grown to a

thickness of 200 nm. A layer of SrRuO$_3$ between the substrates and the superlattice films

acted as a bottom electrode. The top electrodes were circular Pt pads 100 μm in diameter,

deposited on 200 μm centers in a square grid.

2.3 Laboratory X-ray Generator and Diffractometer

We used an x-ray characterization instrument consisting of a rotating anode x-ray

generator and four-circle x-ray diffractometer to make preliminary structure

measurements of the BFO and BTO/CTO superlattice films. This diffractometer allowed

us to identify reflections produced by these films for further study. In particular we used

it to initially locate the half-order reflections produced by oxygen octahedral rotations in

the BTO/CTO superlattices.

2.3.a. Configuration and basic operation of the laboratory diffractometer

The rotating anode generator produces x-rays via the following process. A voltage

produced by a high-voltage direct-current (DC) power supply is applied between the

rotating copper anode and a tungsten filament cathode. Both are held in vacuum to allow

the propagation of electrons and to minimize the degradation of the anode and cathode.

Electrons are emitted from the cathode filament and accelerated towards the rotating

anode. X-rays are emitted when the electrons strike the copper target. The components of

the rotating anode generator are shown schematically in Figure 2.2(a). There are two

physical processes that lead to the generation of x-rays in the copper target: (i)

bremsstrahlung radiation from the rapid acceleration of the electrons upon striking the target and (ii) characteristic radiation from the excitation and relaxation of atomic electrons in the copper anode.

X-ray diffraction using the techniques described in this thesis requires a monochromatic x-ray beam with small spatial dimensions at the sample. The rotating anode generator, however, produces x-rays with a broad range of energies, which are emitted in all directions. The characteristic radiation of the Cu target is sharply peaked at energies determined by the electronic structure of Cu. The experiments described here used the Cu $K_{\alpha1}$ emission line with wavelength $\lambda = 1.5406$ Å .

The diffractometer uses a LiF monochromator and a series of slits to select photons with a wavelength corresponding to the Cu $K_{\alpha1}$ emission line. The monochromator is set so that the Cu $K_{\alpha1}$ radiation meets the Bragg condition of the LiF (002) x-ray reflection. Photons with other wavelengths are absorbed in the LiF crystal. The Bragg angle relative to the direction of the incoming x-rays from the anode is set by mounting the LiF crystal on a rotation stage. The direction to the sample is determined by a set of slits defining the path from the crystal to the position of the sample. The slits after the monochromator also blocked the $K_{\alpha2}$ emission line, which is sufficiently close to Cu $K_{\alpha1}$ in energy that it cannot be fully rejected by the relatively broad angular widths of x-ray reflections from the LiF monochromator crystal.

The LiF monochromator was bent to a radius of 8 inches in order to focus the x-ray beam vertically at the center of rotation of the x-ray diffractometer. A diagram of the x-ray beam path from the anode to the detector is shown in Figure 2.2(b). It is important to note that the LiF monochromator configuration shown in Figure 2.2(b) does not prevent

photons with twice the K_α energy from reaching the sample. The LiF monochromator crystal has allowed Bragg reflections at indices (0 0 2n), and the Bragg condition can thus be satisfied by photons with energy corresponding to an integer multiples of the K_α energy.

The orientation of the sample and the angle between the incident beam and the detector were set using a four-circle diffractometer (Huber Diffracktionstechnik, GmbH). The diffractometer and monochromator were contained in an enclosure designed to prevent accidental exposure to x-rays scattered out of the incident beam. The diffractometer can rotate a sample about three axes, and has an additional motorized rotation arm for the detector. The four angular rotations are motorized and can be controlled with a computer. Additionally, the goniometer heads that hold the samples allow us to make adjustments to the position and orientation of the sample by hand. The goniometer allowed the sample to be simultaneously in the geometric center of the rotation of the four circles of the Huber diffractometer and at the center of the incident x-ray beam.

After leaving the sample, the outgoing diffracted beam passes through a set of slits on the detector arm to reduce the background count rate due to the scattering of x-rays from the air. A second set of slits is used to define the angular acceptance with which scattered x-rays reach the detector. The angle between the center of these slits and the incident beam defines the diffraction angle 2θ. Photons that pass through the detector slits reach the detector.

We used two different detectors. The first of these is a silicon p-i-n diode (Amptek, Inc.) designed as a detector for x-ray fluorescence experiments. The p-i-n diode
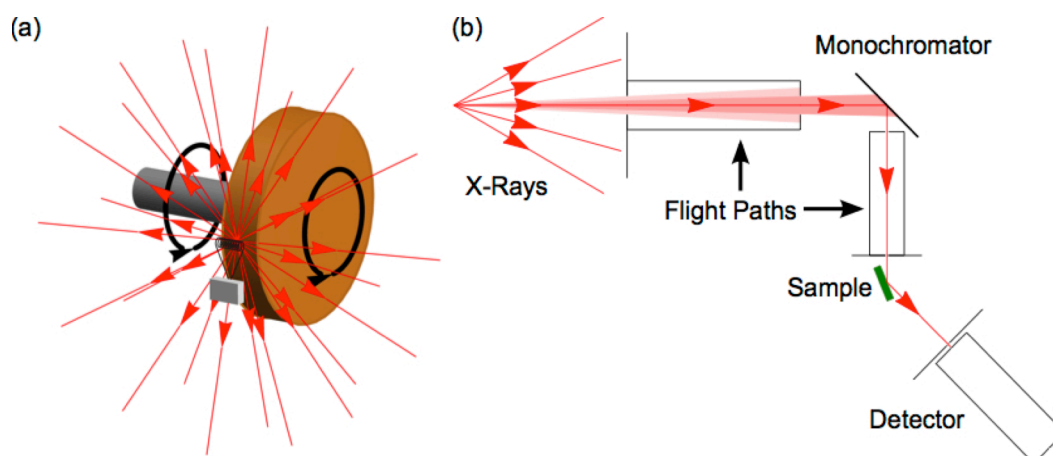
Figure 2.2 (a) Rotating anode x-ray generator. Electrons are accelerated from the tungsten filament cathode to the copper anode, generating x-rays at the anode. (b) Diagram of the x-ray diffractometer described in this section. The x-rays generated by the rotating anode are emitted into a very large solid angle, so slits are used to limit the acceptance of the instrument to a narrow cone of x-rays. A LiF crystal is used to select the Cu $K_{\alpha 1}$ wavelength and to focus the beam at the sample. The flight paths are evacuated in order to minimize scattering and attenuation in the air.

was capable of measuring the energy of each detected photon but had limited dynamic range, with a maximum count rate of less than 10^4 counts/s. The second detector is a scintillation detector (Bicron, Saint Gobain, Inc.) with a greater range, a maximum count rate of approximately 5×10^4 counts/s, but poor energy resolution. In each case detected x-rays produce a voltage pulse with a magnitude proportional to the energy of the detected photon. This signal from is sent to a single channel analyzer (SCA), which in turn produces digital pulses for incident pulses with pulse heights (and thus detected photon energies) within a set range. The SCA was configured to produce counts only for photons near the Cu K_α energy. A particularly important function of the energy selection by the SCA was to eliminate counts due to photons with integer multiples of the Cu K_α photon energy that would reach the sample from the monochromator. The voltage pulses from the detector, before processing by the SCA, were also sent to an oscilloscope in

order to provide an immediate visual indicator of the photon intensity reaching the detector.

We used a software package called spec (Certified Software, Inc.) to control the motion of the four axes of the diffractometer and to record the x-ray intensities from the detector. This software has several useful features for performing diffraction measurements. An angular scan can be programmed by inputting the angle or angles that the scan will vary, the range over which the angle(s) are to be varied (either in absolute terms or relative to the current configuration), the number of intervals into which the scan is to be broken, and the length of time over which intensity is to be counted at each point in the scan. The spec program performs the scan by moving the motor(s) to each angular point in the scan and recording the intensity, along with the position of each motor at that point, the count time, and the index of that point in the scan (0, 1, 2, etc.). The software can also compute reciprocal lattice coordinates for a crystal based on the lattice parameters and symmetry of the crystal, the x-ray photon wavelength, and two (non-parallel) reference positions in reciprocal space. Once the orientation of the crystal with respect to the diffractometer is determined, the software can be used to either find the angular settings corresponding to a set of reciprocal space indices ($H\,K\,L$), or to find the reciprocal space coordinates at a given angular configuration. It can also be used to perform scans along straight lines in reciprocal space (e.g. from $H = .95$ to $H = 1.05$).

The sample was mounted to the goniometer head using double-sided adhesive tape. Other adhesives commonly used for this purpose include modeling clay and nail polish. These other methods have clear drawbacks: Clay is messy and not easily leveled. Removing a sample attached using nail polish risks chipping the sample. After pressing

the sample onto the tape using a pair of tweezers, we held the goniometer head upside down and shook it for a few seconds, to make sure the sample was firmly attached and would not fall off during a measurement. Finally we mounted the goniometer head onto the diffractometer, placing it in its socket and screwing down the base.

The process of aligning the diffractometer required passing the incident beam directly into the detector, so the alignment was performed at the minimum power setting of the x-ray generator (20 kV, 10 mA). In addition, an attenuator consisting of 16 layers of aluminum foil was placed in front of the detector, which reduced the intensity by a factor of approximately 150. Together, these steps allowed the detector to be moved into the path of the direct beam while keeping the count rate at the detector within its dynamic range.

The alignment of the diffractometer for each sample consisted of finding the zeros of two angular axes: the 2θ (detector) angle and θ (sample incident beam angle). In order to align the system we first moved the θ and 2θ angles to their nominal 0° positions and lowered the sample height so that it did not block any part of the x-ray beam. Then we performed a 2θ scan to find the 2θ angle at which the detector registered the highest intensity, indicating the center of the beam. We set this new 2θ angle to 0°, and noted the peak intensity, which was usually 2400 counts/s under the conditions described in the previous paragraph.

To check the θ alignment, we moved the χ angle to 90°, so that the face of the sample was vertical. Next we raised the sample height until the detected intensity was reduced to half the maximum intensity of the direct beam. We then performed a wide θ

scan, over a range of ±1° at least, to find the θ angle of maximum detected intensity. We moved θ to this angle, and repeated these two steps – adjusting the sample height so that it blocked half of the intensity of the direct beam, then doing a θ scan and moving θ to the angle corresponding to the peak of that scan – until the maximum intensity in a θ scan was half the maximum intensity. The software was then set to consider this angle to be θ = 0°.

A subsequent series of steps was required to find the orientations of the crystallographic directions within the sample. The initial step in the orientation process was performed using the extremely strong (0 0 2) reflection from the STO substrate. The angles of the substrate (1 0 1) and (1 1 1) reflections were then found to complete the orientation. The nominal angles of the STO substrate (0 0 2) reflection were θ = 23.23°, 2θ = 46.45°, and χ = 90°.

Under certain angular settings it is possible to produce a collision between the 2θ arm holding the detector and the rotation stage that is used to control the χ angle of the sample. In order to avoid collisions it is necessary to restrict the value of the 2θ angle of the laboratory diffractometer to be no more than 25° greater than value of the θ angle. It is important to consider this limitation when moving between x-ray reflections. The process of avoiding collisions is further complicated because the θ and 2θ stages rotate at different speeds. With these considerations in mind we developed a procedure for moving the diffractometer that avoided collisions. In order to reach the configuration that would allow us to measure the substrate (0 0 2) reflection, for example, we first moved 2θ halfway, to 23°, then moved θ to 23.23, then moved 2θ the rest of the way to 46.46°.

The process of finding substrate (0 0 2) involved a search through the set of angles controlling the sample orientation. The sample alignment on the sticky tape on the goniometer head is uncertain, so the final θ and χ values differed significantly from their ideal values. The 2θ value, however, would not be affected by this uncertainty, so we would expect the initial 2θ angle to be very close to its final value. The uncertainty in the initial alignment of the angle χ was approximately 1° on either side of its nominal 90° starting point. The angular resolution in that direction is poor, however, approximately 1° full-width at half maximum (FWHM). The poor resolution in χ arises from the divergence introduced by the vertical focusing of the LiF monochromator and the large vertical slits and the detector required to collect the diverging beam after the sample.

Weak tails of the intensity from the substrate (0 0 2) Bragg reflection were distributed through a small range of angles. Our strategy for finding the Bragg reflection was to first search across a wide range of angles to find a weak tail. We then used an iterative process to close in on the center of the reflection. First we did a θ scan and moved θ to the peak position from that scan. Then we did a χ scan, and moved χ to that peak. Finally, we did a $\theta/2\theta$ scan, in which 2θ is changed by twice as much as θ between each point in the scan, and moved 2θ to the peak from this scan. We repeated these three steps until the peak angles stopped changing, indicating we had arrived at the center of the reflection. We then noted the final angle values, and used them as the 0 orientation point in spec's orientation matrix (with a = b = c = 3.905 Å, $\alpha = \beta = \gamma = 90°$, and (H K L) = (0 0 2) for this point). We also noted the θ offset $\omega = \theta - (2\theta)/2$.

To complete the sample orientation, we then found the substrate (1 0 1) and (1 1 1)

reflections. First, to find the (1 0 1) reflection, we moved 2θ to its calculated value, θ to

(2θ)/2 + ω, χ to 45°, and left φ at 0°. Like θ for the preceding reflections, the peak in φ is

relatively narrow. And, since the φ orientation was initially set by eye, we would not

expect to find any intensity at the initial angle values. We therefore started with a wide

(± 2°) φ scan, during which we watched the oscilloscope for an increase in count rate in

case the φ interval was wide enough that the peak fell between two points in the scan.

Once we found part of the substrate (1 0 1), we closed in on the reflection using the angle

scan sequence φ, χ, θ/2θ. We then noted the final φ value, which we used as a fixed φ

offset ϕ_{off} for all subsequent measurements of off-axis reflections. Finally, we looked for

the substrate (1 1 1) reflection, moving θ, 2θ, and χ to calculated values, and φ to

45° + ϕ_{off}. We used the scan sequence θ, χ, θ/2θ to close in on the reflection, and used the

final angle values for the 1 orientation value in the spec orientation matrix.

2.3.b. Specific methods for the study of weak x-ray reflections

The x-ray reflections associated with the rotation of oxygen octahedra in the

BTO/CTO superlattice are particularly weak. Relative to the intensity of the BTO/CTO

superlattice (0 0 2) reflection, we expect the intensities of the half-order reflections to be

lower by a factor of 2 orders of magnitude less in the case of the (3/2 1/2 1/2) reflection,

and 4 orders of magnitude in the case of the (3/2 1/2 1) reflection. Searching for these

reflections is a challenging problem, which we addressed by developing a series of

specialized experimental procedures.
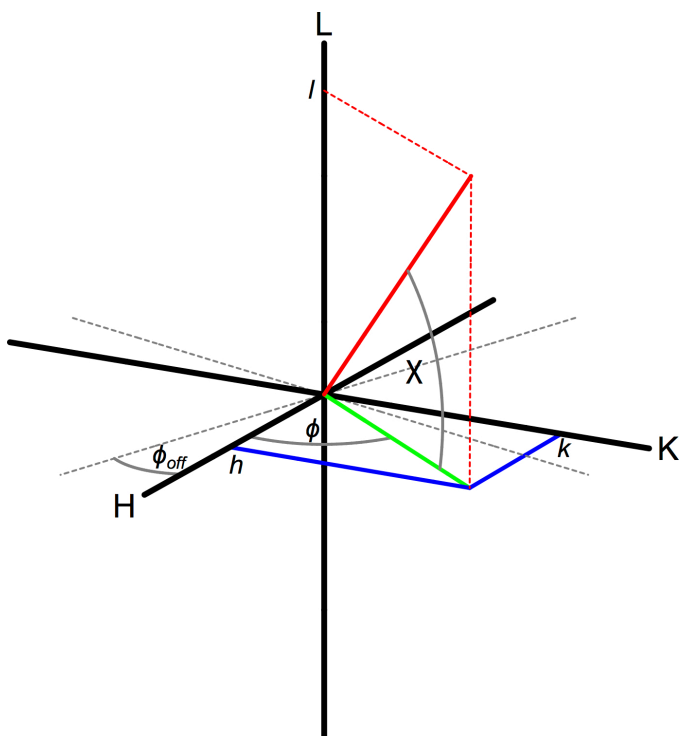
Figure 2.3 Diffractometer angles associated with a reciprocal lattice vector with indices (h k l). χ is the angle between the vector and the *H-K* plane, and ϕ is the angle between the *H*-axis and the projection of the vector onto the *H-K* plane. ϕ_{off} is the angle by which the sample is rotated about the ϕ-axis on the goniometer head. 2θ (not shown) is determined by the magnitude of the vector, using Bragg's law. This illustration shows a symmetric diffractometer configuration, in which $\omega = 0$ (i.e. $\theta = (2\theta)/2$).

The first step in finding the half-order x-ray reflections arising from octahedral rotations was to find the (0 0 2) x-ray reflections of the superlattice thin film, in order to determine the ratio of the out-of-plane lattice parameter of the STO substrate ($c_{sub} = 3.905$ Å) to the lattice parameter of the superlattice thin film (c_{SL}).

Due to the relative ease of performing computations based on a cubic lattice structure, we used reciprocal lattice indices based on the cubic crystal structure of the STO substrate, rather than the structure of the superlattice film. In order to find the (0 0 2) reflections of the superlattice, we set the diffractometer for the angles associated with the substrate (0 0 2) and performed a wide-range $\theta/2\theta$ scan. The wide $\theta/2\theta$ scan shows multiple peaks, including the substrate (0 0 2), which has the highest intensity, the superlattice pseudocubic (0 0 2), which is second highest, and possibly one or more additional reflections from the superlattice, which are less intense. We moved θ and 2θ to the superlattice (0 0 2) from this scan, and used the same iterative process to close in on the center of this reflection.

We then noted the final angle values for the superlattice (0 0 2), and used the final 2θ

value to compute the ratio of the out-of-plane lattice constants of the substrate and

superlattice.

After carrying out this orientation procedure, we could find half-order superlattice

reflections. To find the superlattice (3/2 1/2 1/2) reflection, for example, we first

converted those superlattice reciprocal lattice unit (r. l. u.) indices into substrate r. l. u.

indices, using:

$$\vec{H} = (h\ k\ l) = \left(\frac{3}{2}\ \frac{1}{2}\ \frac{1}{2} \cdot \frac{c_{sub}}{c_{SL}}\right)$$

The substrate r. l. u. values were used to estimate the angles where the (3/2 1/2 1/2)

reflection would be found. The definitions of the angles are shown graphically Figure

2.3. The values of the angles can be determined from h, k, and l using:

$$\phi = \tan^{-1}\frac{k}{h} - \phi_{off} = \tan^{-1}\frac{1}{3} - \phi_{off}$$

$$\chi = \tan^{-1}\left(\frac{l}{\sqrt{h^2 + k^2}}\right) = \tan^{-1}\left(\frac{c_{sub}/c_{SL}}{\sqrt{10}}\right)$$

$$2\theta = 2\sin^{-1}\left(\frac{\lambda \cdot \|\vec{H}\|}{2 \cdot c_{sub}}\right) = 2\sin^{-1}\left(\frac{1.54\ \text{Å} \cdot \sqrt{\left(\frac{3}{2}\right)^2 + \left(\frac{1}{2}\right)^2 + \left(\frac{1}{2} \cdot \frac{c_{sub}}{c_{SL}}\right)^2}}{2 \cdot c_{sub}}\right)$$

$$\theta = \frac{(2\theta)}{2} + \omega.$$

Here ϕ_{off} measures the azimuthal misorientation of the sample with respect to the φ

rotation stage of the diffractometer. After moving to these calculated values, we increased

the x-ray power to maximum using the following sequence, with pauses of two minutes

between changes:

20 kV	10 mA
35 kV	10 mA
50 kV	10 mA
50 kV	40 mA
50 kV	70 mA
50 kV	100 mA

.

With the x-ray intensity at maximum we began to search for the intensity signature of x-rays diffracted from the half-order reflections. Due to the low intensities of these reflections, we used count times of at least 10 s. At maximum x-ray power, the background intensity in the vicinity of the (3/2 1/2 1/2) reflections was 2 counts/s. The peak intensity depended on the sequence of layers from which the superlattice was composed, and was at most 15 counts/s (including the background). The signal could be as low as 3 counts/s with the least favorable composition, termed B4C2, consisting of a repeating unit of 4 unit cells of BTO and 2 unit cells of CTO.

In searching for these half-order reflections, we had to find a way to exclude artifacts arising from detecting photons with twice the $CuK_{\alpha 1}$ energy. Note that the wavelength of these photons is half of the $CuK_{\alpha 1}$ wavelength and would be diffracted at the nearly same set of angles as half-order reflections from very strong integer-index substrate reflections. In order to distinguish between the different photon energies we used the p-i-n detector designed for fluorescence experiments, which we termed the fluorescence detector (FD). As a diagnostic measure, we split the signal from the FD and sent it to two SCAs: a primary channel for the Cu K_{α} signal and a secondary channel for

the half-wavelength photon signal. By recording both channels during each scan we were able to check if a region of elevated intensity in the primary channel could actually be from a half-order reflection, because there would have to be a nearby reflection in the secondary channel.

2.4 Synchrotron Radiation Measurements

2.4.a. X-ray diffraction at synchrotron light sources

X-ray light sources based on synchrotron radiation from electrons in an electron storage ring offer many advantages. These light sources produce high-intensity x-ray beams. The x-ray intensity at BL13XU, the beamline we used at SPring-8, was approximately 10^{13} photons/s, compared to the approximately 10^7 photons/s produced by our lab source at maximum power. Unlike our lab source, which can only provide a beam of photons with a wavelength of 1.5406 Å, synchrotron light sources can produce a wide range of photon wavelengths,[26] allowing us to select shorter wavelengths that let us observe higher-index reflections. The photons are emitted in short fixed-duration pulses in which the intensity arrives over a time with a FWHM of 100 ps, and can be focused to a spot size of far less than 1 μm^2.[27] This allows us to make measurements with sub-nanosecond time resolution and sub-micron spatial resolution. The x-ray beam is also highly collimated, affording us greater angular resolution than our lab diffractometer.

In the electron storage rings around which synchrotron light sources are built, bunches of electrons travel at relativistic speeds in vacuum. At the SPring-8 light source, the electron bunches are initially accelerated by a linear accelerator into a booster ring, where their energy is boosted to the desired energy for the electrons in the storage ring.
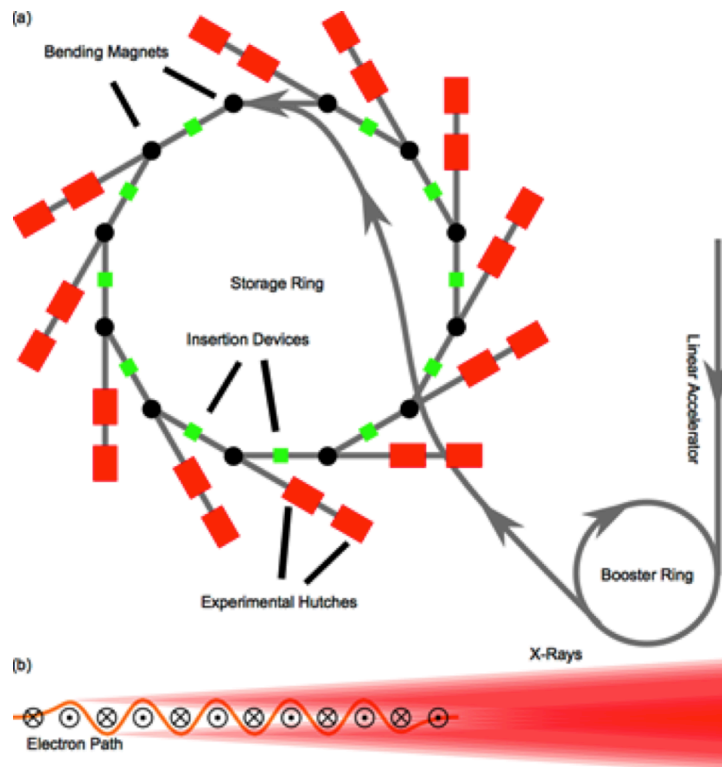
Figure 2.4 (a) Simplified diagram of the electron storage ring x-ray light source at SPring-8. Electrons are accelerated first in the linear accelerator, then in the booster ring, before entering the storage ring. Insertion devices produce magnetic fields with alternating directions, causing oscillations in the paths of the electrons, as illustrated in (b). These oscillations generate x-rays in a narrow energy range determined by the oscillation period. Note that at SSRL, the electrons travel clockwise, rather than counterclockwise as illustrated here.

The electrons are then injected into the main storage ring. A series of magnets set the orbit of the electrons. A diagram of an idealized electron storage ring similar to SPring-8 is shown in Figure 2.4(a). The acceleration due to the magnets that confine the electrons to their orbits results in the emission of electromagnetic radiation in a cone tangent to the path of the electron beam. The radiation emitted at these bending magnets is distributed across a very broad spectrum and a large solid angle.

Other magnetic devices are used to generate photon beams with a narrower energy range, smaller source size, and smaller angular divergence. These devices are inserted in

the straight sections of the storage ring between bending magnets and are termed

insertion devices. Insertion devices create a vertical magnetic field that oscillates along

the path of the electrons, causing the electrons to oscillate horizontally as they pass

through, as illustrated in Figure 2.3 (b). Each oscillation consists of two small bends, so

by including many such oscillations the x-ray intensity produced can be increased many

times over. There are two types of insertion devices: wigglers and undulators, which are

differentiated by the degree of constructive interference between the radiation from

successive periods of the array of magnets within the insertion devices. The narrowest

beams in both spectral width and divergence are produced by undulator insertion devices,

in which the emission from each magnetic period interferes constructively only within a

narrow range of wavelengths in a narrow cone.[28] The electron oscillations caused by an

undulator magnet produce radiation that is in phase for a particular photon energy and

odd integer multiples thereof, causing the radiation amplitudes, rather than intensities, to

be added.

2.4.b Measurements at SSRL

A series of measurements of the zero-electric-field structure of the BTO/CTO

superlattices were performed at SSRL. The beamline we used at SSRL, 10-2, uses a

wiggler insertion device, which produces an intensity that is the sum of the intensities

produced by each separate oscillation the electrons undergo. The wiggler was set to

produce an x-ray beam with a photon energy of 20 keV (wavelength $\lambda = 0.6199$ Å). The

precise beam energy is selected from the broad range of photon energies produced by the

wiggler insertion device using a Si (1 1 1) double-crystal monochromator. This Si (1 1 1)

Figure 2.5 Diagram of a synchrotron x-ray beamline. The double-crystal monochromator transmits a narrow range of wavelengths. Filters attenuate the beam if necessary. A small focal spot is produced at the sample using x-ray mirrors in the Kirkpatrick-Baez (KB) geometry.

monochromator has a different series of harmonics than the LiF monochromator described in section 2.2. Silicon's diamond F.C.C. crystal structure produces reflections only at indices ($h\ k\ l$) where h, k, and l are all odd, or all even and sum to a multiple of 4. This relatively sparse set of allowed reflections reduces the complications arising from harmonics of the primary photon energy. For example, the location of the (1 1 1) reflection for 20 keV photons is where the (2 2 2) reflection for 40 keV photons would be. Bu but since the sum of the indices $2 + 2 + 2 = 6$ is not a multiple of 4, this particular reflection is not allowed. The Si (1 1 1) monochromator instead produces harmonics due to the Si (3 3 3) reflection at energies a factor of three higher than the base 20 keV photons.

After passing through the monochromator, the x-ray beam at station 10-2 of SSRL is focused vertically and horizontally using Kirkpatrick-Baez (KB) mirrors. The beam then passes through a set of filters that can be switched in and out to reduce the intensity in order to limit the beam-induced damage to the sample or to keep the diffracted x-ray intensity within the dynamic range of the detector. The sample is

mounted on a six-circle diffractometer (Huber Diffracktionstechnik, GmbH). Figure 2.5

shows a diagram of this beam path. The diffracted x-rays are detected using either a two-

dimensional pixel array detector (PAD) (Pilatus 100K) or a scintillation counter. The two

detectors are mounted on the same detector arm, separated by a fixed angle. By moving

the detector arm back and forth by this angle we could switch between the two detectors.

Once the x-ray beam had been focused, we performed a 2θ alignment check similar

to the procedure used with the lab diffractometer and described in section 2.3.a. We used

the scintillation counter to find the center of the direct beam, and set that 2θ angle to 0°.

Then we rotated the detector arm (2θ) up by the 30° offset between the PMT and the

PAD, and noted the pixel coordinates on the PAD that corresponded to center of the

beam. We then performed a θ and sample-height alignment procedure. This procedure

was also very similar to the one described in section 2.3.a, with the exception that the

sample height was also being set by a translation stage controlled using the spec program.

This motor allowed us to perform sample-height scans rather than making manual

adjustments.

We used a different set of x-ray reflections from the STO substrate to orient the

sample than were used with the laboratory diffractometer, due to the higher photon

energy during the SSRL experiment. We first computed the location of the substrate

(0 0 4), and found it. This process was made quicker by the use of the PAD, which

reduced the need for wide initial scans to find some part of the reflection. We set the

substrate (0 0 4) as the 0 orientation point for spec, then found the substrate (1 1 5) and

set that as the 1 orientation point. From there we found the (2 2 4), and then the (4 4 4)

which we used as the final 1 orientation point for spec. We used spec's orientation matrix to perform linear scans in reciprocal space (*h k l* scans), in addition to angle scans.

We had already measured the ratio of the apparent c-axis constants of the substrate and the B2C4 superlattice on our lab diffractometer, but we checked again to make sure. We used the same procedure as before, comparing the 2θ values of the substrate and superlattice (0 0 2) reflections. We also measured the intensities and the FWHM in *h*, *k*, and *l* of these two reflections to have points of reference for the half-order reflections.

To find the half-order reflections at SSRL, we used a different procedure than described in section 2.3.b for the laboratory diffractometer. Instead of computing and going to the initial angles for e.g. the superlattice (3/2 1/2 5/2) reflection, we would first find the superlattice (1 0 2) and (2 1 3) reflections, which are more intense, and perform an *hkl* scan (a scan along a straight line in reciprocal space) between them. If we did find an intensity peak near the center of the scan, we would then move there. If we did not, we would then move to the halfway point and use the two-dimensional PAD to look for a nearby reflection.

In addition to the substrate and superlattice Bragg peaks, we could also use the (3/2 1/2 1/2) and (3/2 1/2 1) reflections, which we measured first, for comparison with the other half-order reflections we observing for the first time. Since we had previously confirmed the presence of the (3/2 1/2 1/2) and (3/2 1/2 1) reflections on the laboratory diffractometer we could more confidently identify candidate peaks as these reflections during this experiment. We compared peak intensities and widths, especially in the *l* direction, to those of the superlattice (0 0 2), as well as the (3/2 1/2 1/2) and (3/2 1/2 1), and excluded reflections with intensities greater than that of the (3/2 1/2 1/2), and

reflections with widths closer to that of the (0 0 2) than of the other half-order reflections. Once we found a peak we believed to be from a half-order reflection, we would close in on the center of the reflection first using an angle scan sequence, and then using h, k, and l scans. Once we found the center, we would note the peak intensity of the reflection, and its FWHM in h, k, and l.

2.4.c Measurements at SPring-8

We used the BL13XU beamline at SPring-8, which is based on an undulator x-ray source. The undulator was set to produce an x-ray beam with a photon energy of 12.4 keV ($\lambda = 1.00$ Å). BL13XU uses a Si (1 1 1) double-crystal monochromator to select the 12.4 keV photons, and Si compound refractive lenses to focus the x-ray beam to a spot size of 3.6 μm in both the horizontal and vertical directions. The diffractometer setup we used for our experiments at BL13XU included an additional three-axis translation stage mounted on the goniometer, as shown in Figure 2.6. This fine positioning stage allowed us to move the samples relative to the x-ray beam in order to position the x-ray beam on particular top electrode pad that we could then contact with the probe tip. The BL13XU experiments also used a 2D pixel array detector (PAD) (Pilatus 100K).

In order to align the sample stage we mounted the sample using nail polish as an adhesive, and performed the iterative θ and sample height positioning procedure described in section 2.3.a. Once we had re-zeroed θ and 2θ and found the correct sample height, we computed and found the substrate and film (0 0 2) reflections of the samples.

For the B2C4 sample, the film (0 0 2) was the (0 0 2) reflection arising from the average atomic spacing of the superlattice thin film. After finding this reflection, we

computed and found the (3/2 1/2 1) reflection. Since this reflection is not on the specular (0 0 L) rod, and is elongated along the L direction, we expected it to appear as a point of elevated intensity that would move along a linear, non-vertical path as the sample was rotated in θ. This path would be at a specific angle relative to the detector pixel grid. We computed this angle to confirm that the reflection we found was indeed the superlattice (3/2 1/2 1) reflection.

The BFO film, in contrast, produced separate reflections from each of its different phases near where the reflection with pseudocubic indices (0 0 2) is found in reciprocal space. We found the T phase (0 0 2) first, but using a 2D detector allowed us to observe the nearby off-axis T_{tilt} (0 0 2) reflections simultaneously. We performed a wide θ scan to identify and match the different reflections with BFO phases.

An overhead camera mounted above the sample facilitated the positioning of the sample so that the x-ray beam fell on the sample electrodes. The camera allowed us to see both the probe tip and the electrodes. We found the edges of the sample using wide sample x and z position scans: at the position in the scan where a reflection from the film disappears we marked the location of the corresponding edge on the screen showing the camera feed, using a marker and a piece of transparent tape. Finding two perpendicular edges allowed us to identify the point on the screen that corresponded to the x-ray position on the sample. We could thereafter visually align the positions of the x-ray footprint, top electrodes, and probe tip.

The metal top electrodes also produced x-ray reflections near the film reflections we were studying. These electrodes were polycrystalline, however, so rather than producing point reflections in reciprocal space, they instead produced spherical reflection
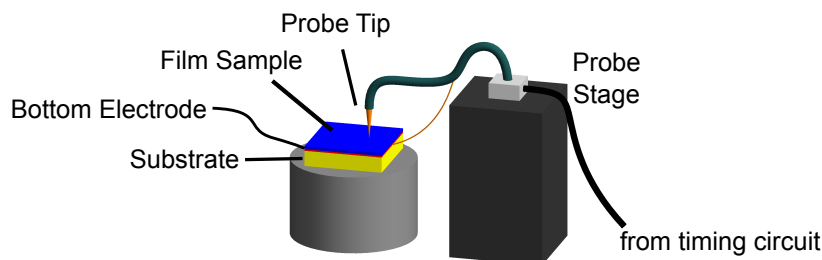
Figure 2.6 The sample stage for electric field response measurements. The probe tip can be translated in three dimensions with the probe stage to make contact with an electrode. The grounded shield electrode of the probe tip is connected to the bottom electrode layer by a wire soldered to the sample.

shells that appeared as rings in our detector images. The Pt (0 0 2) ring is near the B2C4 (3/2 1/2 1) reflection, and the Au (1 1 1) ring is almost on top of the BFO T phase (0 0 2). By recording the intensity from the location of these powder rings alongside each measurement we made, we were able to check later to see if the x-ray footprint was on an electrode during our measurements.

To contact the probe tip to an electrode, we first chose an electrode from a map or photo of the electrode array made or taken earlier. We raised the probe tip and moved it into view of the camera. We then moved the sample stage in small (200 μm) steps to bring the x-ray spot towards the chosen electrode, moving the probe tip over after each step to keep it in view. Once the x-ray spot was on the electrode, we positioned the probe tip over the electrode as well. We gradually lowered the probe tip, occasionally correcting its in-plane position if it appeared to be moving away from the electrode, until we saw the tip slip slightly to the side. This shift indicated that the tip had contacted the electrode.
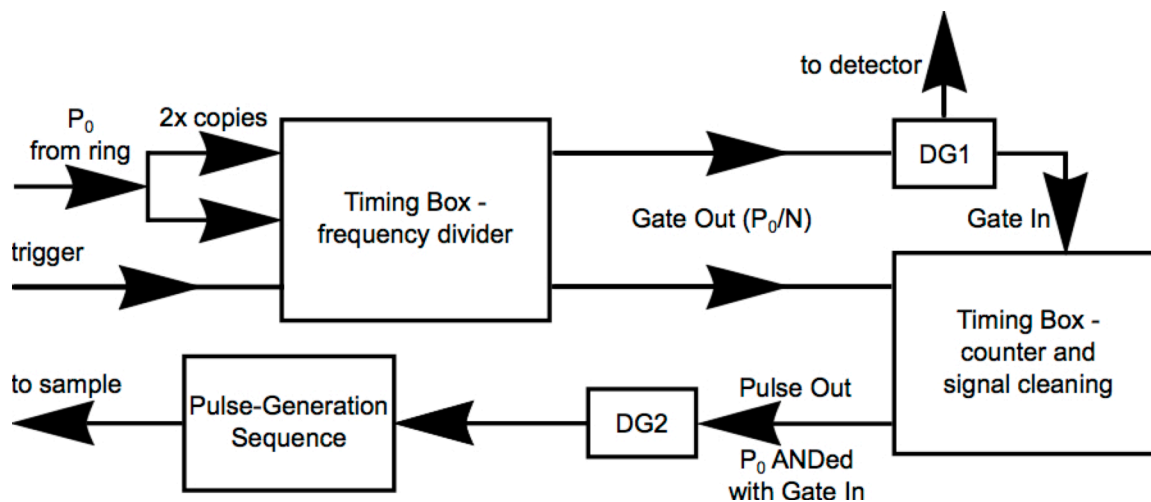
Figure 2.7 Configuration of the timing circuit to perform time-resolved diffraction measurements. The circuit synchronizes the voltage pulses applied to the sample with the gating of the detector and the arrival of an x-ray pulses at the sample by varying the delays produced by the delay generators (DGs). The interval between pulses is selectable at integer multiples of the duration of an electron bunch's circuit of the storage ring.

Once we had brought the probe tip into contact with the top electrode, we could begin the process of adjusting the times of the electrical signal gating the detector and electric field pulse to the sample. We used a timing circuit designed by Alexei Grigoriev,[29] that allowed us to use a signal, P_0, at the frequency of the storage ring to synchronize the PAD exposure window to the arrival of one electron bunch, and to send out a train of a controllable number of electric pulses at a fraction of the P_0 frequency to a function generator or pulse generator. A diagram of this circuit is shown in Figure 2.7.

There are three parameters for the timing circuit that can be set – the frequency divisor N, the pulse width, and the number of pulses to be applied. The timing circuit takes one copy of the P_0 signal and, when it receives a trigger from an external source, sends out a signal with frequency P_0/N. This signal is split into two, with the first copy going to a counter in the timing circuit that counts up to the set number of pulses, and the other going to a delay generator. The delay generator sends one delayed copy of the P_0/N

signal to the Pilatus. A second copy is delayed by a different amount such that it overlaps with the P_0 signal. The timing circuit sends out a signal during the overlap of this second copy and a clean copy of the P_0 signal until the counter exceeds the chosen number of pulses. The output signal is delayed by a second delay generator, then sent to a pulse generator.

Two different pulse generators were used to produce the voltage pulses applied to the samples. A fast pulse generator (Agilent A8114) was used to generate short pulses with durations of 2 µs or less. Experiments with longer-duration pulses on the order of 1 ms used a digital function generator followed by an amplifier.

A series of steps were used to synchronize the PAD with the arrival of a pulse of x-rays from a single electron bunch in the storage ring. First the PAD was switched from its internal gating mode to the external enable mode, in which the detector counted x-rays arriving only during an exposure window set by a digital voltage signal from one of the delay generators. The external gating mode excluded all of the intensity that would have come from the other electron bunches. We also set the PAD to save an image of the detected intensity when the voltage pulse train to the sample was complete. To do this we set the PAD software to combine multiple exposures, up to the number of voltage pulses applied to the sample, into one image.

The appropriate time for the gating signal was determined by scanning the time delay of the pulse to the external enable signal of the PAD. The output of this scan was an alternating sequence of high intensity and low or zero intensity, corresponding to x-ray pulses from different electron bunches, and the time between bunches. We chose a delay

time corresponding to an intensity peak, noted it, and set the delay generator to that delay time for the rest of the experiment.

To determine the appropriate time for the arrival of the voltage pulse at the samples, we first went to a reflection that would reveal a piezoelectric response in the film. This reflection was the (002) Bragg reflection of the BTO/CTO superlattice and the T phase (0 0 2) reflection for the BFO. We would either stay at the center of this reflection, or rotate the sample to a point halfway down the peak in θ. We then moved an electrode into the x-ray beam and made contact with the probe tip. We assigned a region of interest (ROI) to an area in the detector images that corresponded with the reflection, and did a wide scan of the delay to the pulse generator. We looked for a change in the ROI intensity as a function of time and noted the largest delay time that showed a change. The change in intensity could be a decrease if the θ angle was set at the maximum point of the θ scan or on the high-θ side, or an increase if the θ angle was set to the low-angle side of the peak in the θ scan. Note that the longest delay time corresponded to the delay at which the voltage pulse arrived just before the x-ray pulse reaches the sample. This time was set as time-zero.

Once we had completed these spatial and temporal alignment procedures, we could begin to measure the response of our samples to the application of electric fields. To study the response of the oxygen octahedral rotations in the B2C4 superlattice film, we re-located the (3/2 1/2 1) reflection and did a series of delay scans. In a delay scan, the delay to the pulse generator applying the electric field to the film is varied. At low delay times, the pulse is applied long before the x-ray pulse from the electron bunch arrives, so the exposure takes place long after the pulse is applied. At high delay times, the field is

applied after the exposure is taken. Delay scans can be thought of as going backwards in time.

We made measurements of the response of the sample to short-duration (< 1 μs) and long-duration (> 1 ms) voltage pulses of different magnitudes and waveforms. Before and after each measurement we would confirm that the voltage pulses were still being applied by examining the piezoelectric shift of the superlattice (0 0 2). Each measurement consisted of a series of repeated scans of the delay time, usually 10 scans. The advantage of repeating the scan rather than simply counting longer at each point was that the repetition allowed us to recover information from partially completed measurements, which would occur for example in the event of a disruption in the stored electron beam.

To process our measurements, we sorted the detector images by delay time for each scan, and summed the images as an array of pixel intensities for each delay time. We defined ROIs for the location of the (3/2 1/2 1) reflection and for the background. The images were converted into lists of pixel coordinates and intensities (x, y, n) for each summed image. We calculated the total intensity in each ROI for each delay time, and normalized by the average (3/2 1/2 1) reflection intensity from the times before the pulse was applied.

Our measurements of the electric field responses of the BFO film included two types of studies. The first consisted of comparisons of the zero-field diffraction patterns from before and after pulses were applied. To make a static response measurement, we moved to a new capacitor and did a wide θ scan for comparison before applying any voltage pulses. We then applied a series of e.g. 1000 +5 V pulses, and did the same wide θ scan again. We could then go on to apply more pulses of the same voltage, pulses of a

higher voltage, or pulses of a negative voltage. After each series of pulses we did another wide θ scan, allowing us to observe the intensity changes of the reflections from the different BFO phases.

A second series of measurements compared the intensities of the x-ray reflections from the BFO thin films before and during applied voltage pulses. In this case the time-dependence of the change in the intensity was measured as the pulses are being applied. We made two different kinds of dynamic electric field response measurements – a comparison of the change in reflection intensities during the application of different voltages, and a time-resolved measurement of the change in intensity of one reflection as a voltage pulse was being applied. The BFO film reflections were sufficiently intense that scan repetition was not required to accumulate enough photons for good counting statistics. In all of these dynamic measurements, a voltage pulse was applied across the film either before or after each exposure. Therefore, unlike the static measurements which always began with a new capacitor over a presumably hitherto undisturbed region of film, our dynamic measurements were made using regions of the film that had already had thousands of pulses applied to it.

Chapter 3: BaTiO$_3$/CaTiO$_3$ Superlattices

3.1 Introduction

Heteroepitaxial complex oxide superlattices present the opportunity to design materials with phenomena not available in bulk crystals. These can include unusual ferroelectric properties not intuitively derived from the properties of the sub-layers of the superlattice. The properties of these ferroelectric superlattice materials can be studied with high precision using computational methods based on density functional theory.[30] Superlattices can be created using the synthesis techniques that were briefly described in Chapter 2, most commonly with a sequence of two alternating layers.[31] More elaborate superlattices have sequences of three layers, a configuration that permits the creation of structures with symmetries not available with only two components, most notably structures lacking inversion symmetry.[32] Even the periodicity itself can be varied or removed completely,[33] which can be important for selecting the harmonic spectrum in non-linear optical devices.[34]

In terms of basic ferroelectric phenomena, superlattices can present surprising behaviors. It is possible, for example to create superlattices exhibiting antiferroelectric phase transitions from nominally ferroelectric components.[35] Similarly, the structural distortion of interfaces can modify the atomic-scale mechanism of ferroelectricity.[36,37] Very recently, superlattice compositions have been theorized to exhibit a new phenomenon termed hyperferroelectricity, in which thin layers remain polarized even when their depolarization field is not screened.[38]

The basic picture of ferroelectricity in superlattices can be formed first by considering the structure and properties of the compounds from which the sub-layers of the superlattice are formed. This chapter describes detailed studies of the structure and properties of two-component superlattices formed from alternating layers of barium titanate ($BaTiO_3$ or BTO) and calcium titanate ($CaTiO_3$ or CTO) grown on strontium titanate ($SrTiO_3$ or STO) single crystal substrates. The properties of thin films of these materials with uniform composition grown epitaxially on (001)-oriented STO substrates have been described theoretically and probed in experiments. Under the biaxial strain imposed by STO, CTO is predicted to be polarized along in-plane [1 1 0] directions.[39] BTO is polarized along the out-of-plane direction along the surface normal of the substrate. It is also useful to consider thin films of lead titanate ($PbTiO_3$ or PTO) grown on STO, and to compare BTO/CTO superlattices with PTO/CTO superlattices. Thin films of PTO are polarized along the out-of-plane [0 0 1] direction. PTO/CTO superlattices grown on STO can be polarized in either [1 1 0] or [0 1 1] directions, or along intermediate directions of the form [u 0 v] or [u u v], depending on the relative thicknesses of the PTO and CTO layers.[40]

The structure of the interfaces between the component sub-layers, and the strain imposed by the substrate and the component sub-layers on the film as a whole, also influence the electronic properties of the superlattices.[31,37,41] In BTO/STO films, increasing the interface density within the film increases the dielectric constant of the film.[42] In ferroelectric BTO/CTO/STO films, the compressive strain imposed by the CTO and STO layers on the BTO layers increases the ferroelectric Curie temperature.[43] Increased compressive strain has also been predicted to increase the out-of-plane polarization of BTO/CTO superlattices.[44]

The structure of oxide superlattices that incorporate ferroelectric components depends on a competition between electrostatic and structural effects.[12,45-47] The key structural effects include the distortion of the octahedra of oxygen atoms surrounding the central Ti atom of the perovskite building blocks of the superlattice. The oxygen octahedra are distorted, rotated, or tilted with respect to their ideal orientations in the simple-cubic perovskite structure. The rotation of the oxygen octahedra about the out-of-plane axis can reduce or completely eliminate the ferroelectric remnant polarization.[41] The tilting of the octahedra about in-plane axes can reduce their rotation about the out-of-plane axis, however, thereby increasing the polarization of the superlattice film.[44]

Ferroelectric materials are characterized by a remnant electrical polarization. As a result of their polarization, ferroelectrics exhibit a coupling between electrical and mechanical phenomena termed piezoelectricity. One consequence of piezoelectricity is that an applied electric field results in a distortion of the crystal structure such that the induced strain tensor is related to the applied field via a tensor of piezoelectric coefficients. The piezoelectric coefficients are proportional to the magnitude of the

ferroelectric electric polarization. Materials with larger polarizations in general have larger piezoelectric responses.[40,48] The piezoelectric strain in oxide ferroelectrics is typically developed extremely rapidly, such that the strain observed in piezoelectric thin films is often limited only by the characteristic time constant with which charge can be supplied to the electrodes of thin film capacitors.[49]

The degrees of freedom associated with the rotation of oxygen octahedra in complex oxide superlattices, however, can yield disorder that drastically changes the electromechanical properties. Creating the piezoelectric strain in response to an applied electric field requires the progressive relaxation of the system at a series of increasing length scales.[50] The hierarchy of spatial length scales in disordered systems can lead to dielectric responses that are stretched to long times.

We have developed an experiment that allows us to test the relationship between oxygen octahedral rotations and piezoelectric response times in complex oxide superlattices. We use BTO/CTO superlattices, which are piezoelectric and exhibit octahedral rotations, as our model system. We will describe the BTO/CTO system in depth later in the chapter.

Studies of structural change in an applied electric field have previously shown that the piezoelectric response of BTO/CTO superlattices is extremely slow in comparison to that of other oxide ferroelectrics. $Pb(Zr,Ti)O_3$ (PZT) films have characteristic times associated with the piezoelectric response to an applied electric field that are less than 1 ns.[49] A BTO/CTO superlattice consisting of a repeating unit of 2 BTO unit cells and 4 CTO unit cells, termed a 2(BTO)/4(CTO) superlattice, however, exhibits small piezoelectric strain in short-duration applied electric fields. The magnitude

of the strain at a time 300 ns after the beginning of the applied electric field is an order of magnitude smaller than the strain it exhibits after 2.5 ms in response to the same applied field.[14] The experiments described in this chapter test the relationship between these dynamics and the steady-state configuration of oxygen octahedra.

The results of the experiments described in this chapter provide insight into the steady-state structure of the BTO/CTO superlattice and into the response of these structures to applied electric fields. With respect to the steady-state structure, synchrotron x-ray diffraction shows that octahedra within the CTO component of BTO/CTO ferroelectric superlattices are rotated with respect to the tetragonal parent structure. This distortion is observed in a series of superlattices with different sub-layer thickness combinations. The angle of rotation is not uniform within the film. Density functional theory calculations predict that the magnitude of the rotation of TiO_6 octahedra between BaO layers is approximately one order of magnitude smaller than the rotations of octahedra between CaO layers. The small rotation of octahedra within the BTO layers leads to disorder in the directions of oxygen octahedral rotations in adjacent CTO layers. A reversal in the rotation pattern is thus possible at each BTO/CTO interface and the coherence of rotations is limited to a distance corresponding to several perovskite unit cells. The response of the system to applied electric fields incudes changes in the rotation of the oxygen octahedra. The intensities of x-ray reflections arising from octahedral rotations vary in applied electric fields, and have slow dynamics consistent with the steady-state disorder in the octahedral rotation pattern.

3.2 BaTiO₃/CaTiO₃ Superlattices

The superlattices for this study are composed of a sequence of perovskite complex oxide layers with similar structures. The superlattices have nominal compositions corresponding to alternating layers of BTO and CTO, composed of a sequence of BaO or CaO layers separated by layers composed of TiO_2. These studies were conducted at room temperature, where $BaTiO_3$, a ferroelectric material, is polarized along the out-of-plane direction.[51]

The steady-state structure of the $BaTiO_3$/$CaTiO_3$ superlattice can be thought of in terms of a structural compromise. The first element of this compromise is an antiferrodistortive (AFD) instability in the TiO_2 layers between CaO sheets, which leads those oxygen octahedra to rotate slightly about the out-of-plane axis. The second important structural effect is a polar instability that leads the oxygen atoms to shift along the out-of-plane axis, in the opposite direction to the other atoms.[52,53] The relative importance of each distortion depends in turn on the external boundary conditions, including the applied electric field.

Density functional theory (DFT) calculations for a superlattice with a repeating unit of 2 BTO unit cells and 4 CTO unit cells (termed B2C4) predict that the magnitudes of the oxygen octahedral rotations change in an applied electric field.[45] The change in rotation angle is predicted to be greatest for the interfacial oxygen octahedra, those between a BaO sheet and a CaO sheet. The rotation angles of these octahedra would reflect the balance between the influence of the AFD instability in the CTO layers and the polarizing instability in the BTO layers, a balance that would be altered in favor of increased polarization by the application of an electric field. The competition between

these the two key structural effects exists for a range of different numbers of BTO and CTO layers in the superlattice repeating unit.[45] In each case, the octahedra within the CTO layers are expected to exhibit significant rotations about the out-of-plane axis, and the octahedra within the BTO layers are expected to show little-to-no rotation, instead exhibiting polarizing displacements. It is the interfacial octahedra whose disposition is less certain, depending as it does on the balance between these two effects in that particular superlattice.

The experimental details are described in Chapter 2. To summarize briefly, superlattices with B2C4, B3C3, and B4C2 compositions were grown epitaxially. The total thickness of the superlattice thin film was 200 nm, which corresponds to approximately 85 superlattice repeating units. The superlattice was grown on top of SrRuO$_3$ bottom electrodes on (001)-oriented SrTiO$_3$ substrates.[46] Platinum top electrodes were deposited to form thin-film capacitors. The in-plane lattice parameters of the BaTiO$_3$/CaTiO$_3$ superlattices matched those of the SrTiO$_3$ substrates.

Structural studies of the B2C4 superlattice were conducted in zero applied electric field at station 10-2 of the Stanford Synchrotron Radiation Lightsource, using x-rays with a photon energy of 20 keV. Further structural characterization of the entire series of superlattice compositions was performed on our laboratory diffractometer using Cu K$_{\alpha 1}$ characteristic radiation. We studied the structural changes produced by applied electric fields using time-resolved x-ray diffraction at station BL13XU of SPring-8, Harima, Japan.[54] X-rays with a photon energy of 12.4 keV were focused to an area within the Pt top electrode using a compound refractive lens. Diffracted x-rays were detected using a gated two-dimensional pixel array detector synchronized to the applied voltage pulses.[29]

Square voltage pulses with magnitude and duration of 12.5 V and 400 ns were applied

using a pulse generator. Further experiments were conducted with longer-duration pulses

using a triangular waveform with a peak magnitude of 20 V and a duration of 2.5 ms.

3.3 Octahedral Rotations in BaTiO$_3$/CaTiO$_3$ Superlattices

The polarization of the CTO blocks despite the expected presence of oxygen

octahedral rotations causes BTO/CTO superlattices to have persistent polar properties

that are consistent with a uniformly polarized ferroelectric in long-duration electric

fields.[11] The piezoelectric coefficient of the B2C4 film is 54 pm/V in millisecond-

duration electric field pulses,[53] which is similar to the values observed in compositionally

uniform ferroelectric thin films.[55] The dynamics of the piezoelectric response of

BTO/CTO superlattices are puzzling, however, because the piezoelectric strain is an

order of magnitude smaller in nanosecond-duration electric field pulses than in

millisecond-duration pulses.[14] We find that the response of the superlattice to applied

electric field is accompanied by changes in the oxygen octahedral rotations. We observed

these octahedral rotations experimentally in a wide range of BTO/CTO superlattice

compositions, and we found that there is limited long-range order of this rotation pattern.

The disorder in the octahedral rotations contributes to the slowing of dynamics to

timescales that are far longer than the piezoelectricity of compositionally uniform

ferroelectrics.[11]

Several aspects of the structure and functional properties of BTO/CTO

superlattices have been predicted by DFT calculations using methods similar to those

described in Ref. 52. The minimum-energy structure of a B2C4 superlattice, derived from

Figure 3.1 (a) Atomic positions in the B2C4 superlattice unit cell. (b) Magnitude of the rotation of the oxygen octahedra in the corresponding layers. (c) Atomic positions in the TiO_2 layer between the second and third Ca layers of a B2C4 superlattice, indicated by the dashed rectangle in (a), from a structure predicted using DFT in which oxygen octahedral rotations around only the c-axis are permitted. Arrows indicate the handedness of the rotation within an area corresponding to one perovskite unit cell.

DFT calculations constraining the oxygen octahedral rotations to a single axis pointing along the superlattice growth direction, is shown in Figure 3.1 (a). The magnitude and handedness of the rotation is different for the different TiO_2 layers within the B2C4 superlattice, as shown in Figure 3.1 (b). Oxygen octahedra between two CaO layers are predicted to have the largest rotations, ranging from 12.4° to 12.7°. Octahedra between CaO and BaO layers have smaller rotations, with magnitudes of approximately 60% of the rotation of the octahedra between CaO layers. The octahedron between two consecutive BaO layers is rotated by only 0.7°, more than one order of magnitude smaller than the rotation of the oxygen octahedra between CaO layers. The octahedral rotations in DFT calculations are overestimated by both the local density approximation and by the occurrence of oxygen octahedral tilt about in-plane axes, which tends to suppress the rotation.[44] We therefore expect a qualitatively similar variation of the magnitude of the

rotation as a function of the layer composition to be observed in calculations in which oxygen octahedral rotations are allowed to vary about all three axes.

Interfacial octahedra between a BaO layer and a CaO layer are subject to the competing effects of the AFD instability, which is the dominant contribution in CTO, and the polarizing instability, which dominates in BTO. DFT calculations predict that interfacial oxygen octahedra exhibit rotations with intermediate magnitude. The predicted magnitude of the rotation of octahedra between layers of BaO and CaO is less than octahedra between two CaO layers and greater than octahedra between two BaO layers. Because an applied electric field modifies the balance between the competing AFD and polarizing instabilities by making polarized configurations more energetically favorable, we expect these interfacial octahedra to exhibit a greater response than other octahedra in the superlattice to such an applied field.[45] In agreement with this expectation, DFT calculations predict that the magnitude of the field-induced change in the rotation angle of interfacial oxygen octahedra in B2C4 superlattices is a factor of 10 greater than for other octahedra. At an electric field of 105 MV/m the rotations of the oxygen octahedron above the BaO layers are predicted to decrease by 0.8°, and the rotations of the octahedra below the BaO layers are predicted to increase by 0.5°. The rotations of the non-interfacial oxygen octahedra are predicted to be almost unchanged (average of ±0.07°) by the same electric field.[45]

The octahedral rotation pattern is geometrically constrained because oxygen octahedra in neighboring unit cells share an oxygen atom. As a result, a rotational distortion about the out-of-plane c axis in one cell requires a rotation in the opposite direction of the oxygen octahedra of the four in-plane neighboring cells, as seen in Figure

3.1 (c).[56] The directions of octahedral rotations are also predicted to alternate handedness between consecutive TiO_2 layers. The pattern of octahedral rotations can propagate across interfaces between layers of different compositions, as has been predicted for STO/SrFeO$_3$ (SFO) superlattices,[57] STO/LAO interfaces,[58] and some BTO/CTO superlattice compositions.[45] The samples we studied, however, all have compositions that include at least two consecutive BaO layers. We expect that the small octahedral rotations between consecutive BaO layers in our samples leads to short out-of-plane coherence lengths of the rotation patterns, because the thickness of BTO is sufficient to decouple the directions of rotations in successive CTO blocks. Since the rotation of the octahedra between BaO layers is effectively zero, it has no handedness. For these reasons we expect the coherence length of the in-plane rotation pattern to be significantly longer than the out-of-plane coherence length. It is important here to note the distinction between the modulation of the magnitude of the oxygen octahedral rotations within one superlattice repeating unit, and the longer-range out-of-plane disorder that would be the result of this decoupling.

3.4 Relationship between Composition and Intensity of Half-Order Reflections

A systematic variation of the number of consecutive CTO unit cells in the superlattice repeating unit influences the magnitude of the oxygen octahedral rotations. A superlattice with fewer consecutive CTO unit cells has fewer oxygen octahedra with high-magnitude rotations in each superlattice repeating unit. This expectation is consistent with DFT calculations that predict higher polarization in superlattice

compositions with fewer consecutive CTO unit cells,[59] because the oxygen octahedral rotations would reduce the polarization.

3.4.a Detecting oxygen octahedral rotations using x-ray diffraction

The pattern of alternating oxygen octahedral rotations leads to a series of characteristic x-ray reflections due to the effective doubling of the in-plane pseudocubic unit cell.[60] By doubling the size of the real-space unit cell in one direction, the reciprocal space unit cell in that direction is halved. This allows the possibility of half-order reflections - reflections at locations with half-integer indices in the un-halved reciprocal lattice units.

These half-order reflections provide information about the magnitude and coherence of oxygen octahedral rotation patterns. In the experiments described below, reflections in the $\{3/2\ 1/2\ L\}$ family were examined using x-ray diffraction. Different reflections within this family have distinct structural origins. First, the alternation of the directions of the rotations along the c-axis produces reflections in the $\{3/2\ 1/2\ L\}$ family with half-integer L. This pattern of alternating rotation angle signs has odd symmetry, similar to a square wave signal, in that the sign of the rotations alternate with each layer in the following sequence: + - + - + -. As a result of this alternation, the reflections it produces are at odd L indices in the reciprocal space lattice of the expanded unit cell, for example 1, 3, and 5. In terms of the original lattice, the reflections from the alternating octahedral rotation pattern are thus at half-integer indices such as 1/2, 3/2, and 5/2.

The unequal magnitudes of the rotation angles of the six octahedra within the superlattice repeating unit produces a second series of half-order reflections with integer

values of *L*. With equal rotation angle magnitudes, such reflections are forbidden by the symmetry of the unit cell because the reflection amplitudes at integer *L* values are required to sum to exactly zero. DFT calculations predict, however, that the rotation angle is not exactly equal for each octahedron in a superlattice unit. In addition to the differences in rotation angle between octahedra in the CTO layers and octahedra in the BTO layers, the superlattice unit cell net rotation angle (the sum of the signed rotation angles of all six octahedra in the superlattice unit cell) is predicted to be 3.9°, not 0°. The requirement that reflection amplitudes at integer *L* values sum to zero is therefore relaxed, allowing low-intensity reflections at these additional locations.

The DFT calculations by Prof. Wu gave us a set of spatial coordinates for each atom in an expanded superlattice unit cell under different electric fields, one set for each of 17 different fields ranging from 0 to 375 MV/m. We used these coordinates, and the barium, calcium, titanium, and oxygen atomic form factors, to compute the structure factor of the expanded superlattice cell as a function of (*h, k, l*). We then multiplied this function by another representing the approximate size of the film, 10^7 x 10^7 superlattice cells in-plane, and 100 out-of-plane, to get a combined function we could use to find the relative intensities of reflections at different reciprocal lattice indices.

The use of this particular doubled unit cell, rotated by 45° and expanded by $\sqrt{2} \times \sqrt{2}$ in-plane as illustrated in Figure 3.2 (a), elucidated why we had not found reflections at several other half-order locations. Every half-order reflection the superlattice film produces has to be at a reciprocal space location with coordinates that are integers in the reciprocal lattice units of this expanded unit cell. Thus, a location with half-integer indices (*h k l*) in the original pseudocubic reciprocal lattice units, with *h* an integer and *k*
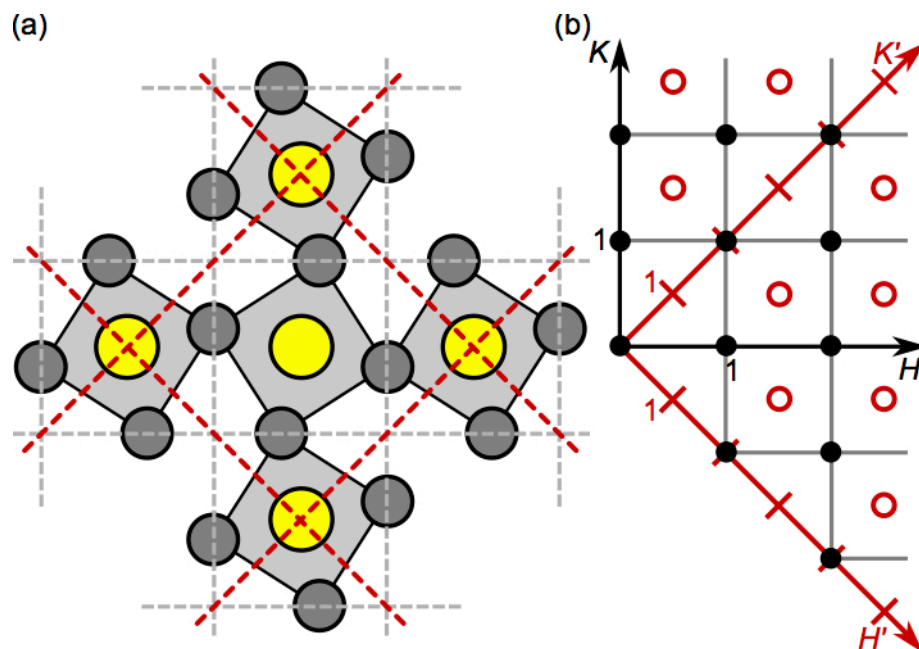
Figure 3.2 (a) Illustration of the unit cell transformation needed to account for the pattern of oxygen octahedral rotations. The borders of the undistorted perovskite unit cells are shown with grey dashed lines, while the expanded and rotated unit cell is indicated with the red dashed lines. (b) Diagram of part of the reciprocal space *HK* plane. The filled black circles indicate locations with reflections produced by the undistorted lattice, while the empty red circles indicate the locations of half-order reflections produced by the octahedral rotations. The black and red axes correspond to the undistorted and expanded unit cells, respectively.

not (e.g. (0 1/2 2)) or vice versa, would not have a reflection because the transformed

reciprocal lattice indices (*h' k' l'*) (which would be (-1/2 1/2 12) in this case) are not all

integers. Figure 3.2 (b) shows the transformation between the reciprocal lattice indices of

the undistorted and expanded unit cells.

Based on these structure factor computations, we predicted that the reflections

with half-integer values of *L*, (3/2 1/2 1/2), (3/2 1/2 3/2), and (3/2 1/2 5/2), would have

intensities that are two orders of magnitude greater than the (3/2 1/2 1) reflection. The

locations of the {3/2 1/2 *L*} and other reflections in reciprocal space are illustrated in

Figure 3.2 (b). We further expect that the intensity of x-ray reflections arising from the

octahedral rotations will vary as the octahedral rotations are modified by the applied
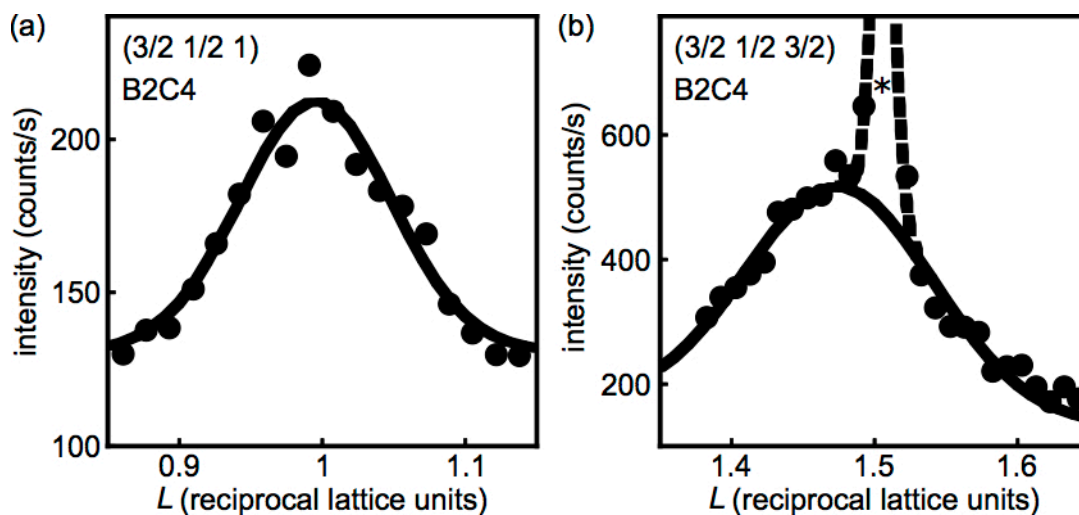
Figure 3.3 (a) X-ray diffraction L scans through (a) (3/2 1/2 1) and (b) (3/2 1/2 3/2) reflections of the B2C4 superlattice. The solid lines are Gaussian fits with FWHM W_L=0.13 and 0.18, respectively. The peak marked (*) in (b) arises from intensity at the location of the (3/2 1/2 3/2) reflection of the $SrTiO_3$ substrate.

electric field. The structural modifications predicted by the DFT calculations would yield a 16% increase in the intensity of the (3/2 1/2 1) reflection in an applied field of 105 MV/m.

3.4.b Half-order reflections from B2C4, B3C3, and B4C2

Radial θ-2θ scans through the (3/2 1/2 1/2) x-ray reflections of the B2C4, B3C3 and B4C2 superlattices are shown in Figure 3.4 (a), (b), and (c), respectively. The presence of this reflection confirms that the vertically alternating rotation pattern predicted in the DFT calculations for B2C4 occurs in all three compositions. The B2C4 and B3C3 compositions produce relatively intense (3/2 1/2 1/2) reflections, while B4C2 produces a weaker reflection. The relative weakness of the half-order reflection for the B4C2 superlattice is consistent with the prediction that the oxygen octahedral rotations are larger between CaO layers and small or absent in octahedra between BaO layers. The corresponding scans through the (3/2 1/2 1) reflection locations are shown in Figure 3.4
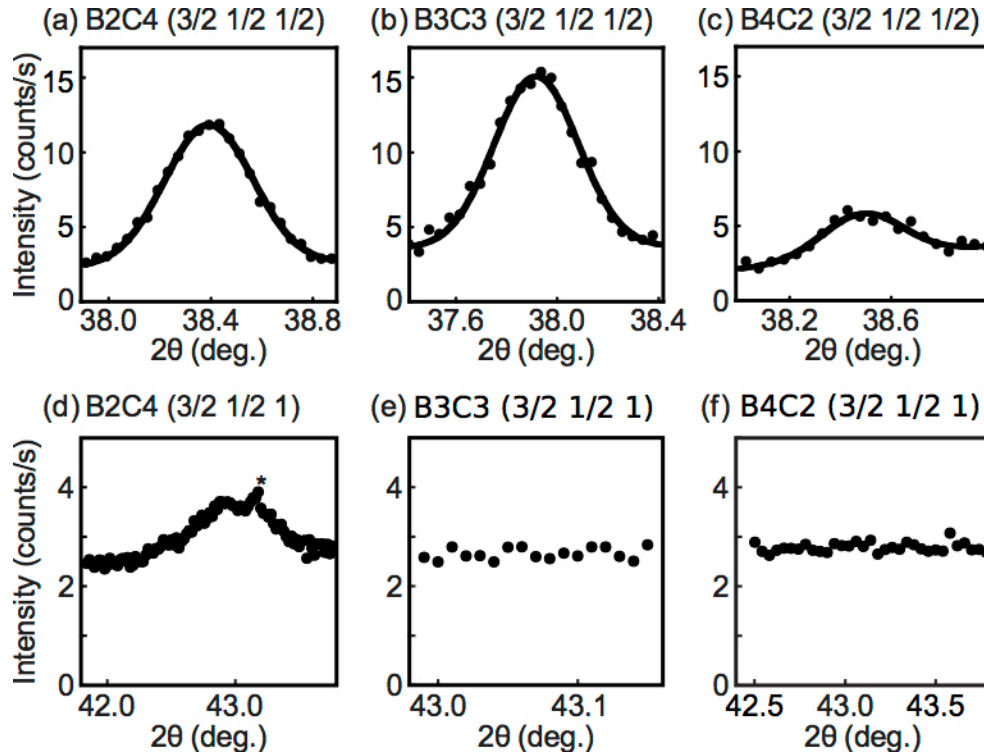
Figure 3.4 θ-2θ scans of (a-c) the (3/2 1/2 1/2) and (d-f) the (3/2 1/2 1) reflections of BaTiO$_3$/CaTiO$_3$ superlattices with compositions B2C4, B3C3, and B4C2. The B4C2, with only two consecutive CaTiO$_3$ layers, has the least intense $L = 1/2$ reflection, and only the B2C4 composition produces a discernable reflection at $L = 1$, which is expected to be weaker. The (*) in (d) indicates the presence of the (3/2 1/2 1) reflection from the SrTiO$_3$ substrate.

(d-f). This B2C4 reflection is less intense than the (3/2 1/2 1/2) reflection, as expected.

The scans of the B3C3 and B4C4 films, which have fewer consecutive CaTiO$_3$ layers

than the B2C4, showed no increase in intensity at this location.

3.5 Disorder in B2C4 octahedral rotations

The widths of the x-ray reflections arising from the oxygen octahedra provide

insight into the coherence of the octahedral rotation pattern. The intensity as a function of

L around (3/2 1/2 L) reflections of the B2C4 superlattice is shown in Figure 3.3 for $L=1$

and $L=3/2$. The full widths at half maximum (FWHM) of these reflections are $W_L = 0.13$

and 0.18, respectively. The widths W_L of these reflections are related to the number of

planes N over which the structure repeats.[28]

The crystal scattering amplitude $F^{\text{crystal}}(\mathbf{Q})$ can be factored into two parts – the

unit cell structure factor and the lattice sum factor:

$$F^{crystal}(\vec{Q}) = \left(\sum_{\vec{n}} e^{i\vec{Q}\cdot\vec{R}_{\vec{n}}} \right) \left(\sum_{j} f_j(\vec{Q}) e^{i\vec{Q}\cdot\vec{r}_j} \right). \qquad (3.1)$$

In one dimension, for a crystal with lattice parameter a and N unit cells, $\vec{R}_{\vec{n}} = na$,

with $n \in \{0, 1, \ldots, N-1\}$. Thus, the lattice sum factor $S_N(Q)$ can be computed as a power

series:

$$S_n(Q) = \sum_{n=0}^{N-1} (e^{iQa})^n = \frac{1 - e^{iQNa}}{1 - e^{iQa}} = e^{iQa\frac{N-1}{2}} \left(\frac{\sin\left(\frac{NQa}{2}\right)}{\sin\left(\frac{Qa}{2}\right)} \right),$$

which, since the scattering intensity $I(Q)$ is proportional to $|S_N|^2$, gives

$$I(Q) \propto \frac{\sin^2\left(\frac{NQa}{2}\right)}{\sin^2\left(\frac{Qa}{2}\right)}. \qquad (3.2)$$

This expression has a peak value of N^2 for $\frac{Qa}{2\pi} = h \in \mathbb{Z}$, and for $Q = \frac{2\pi}{a}(h + \xi), \xi N \ll 1$,

$$|S|^2 \approx \frac{\sin^2 N\pi\xi}{\sin^2 \pi\xi}, \qquad (3.3)$$

giving the approximate intensity distribution around a reciprocal lattice point. This

distribution has a FWHM of approximately $\frac{0.89}{N}$, so the relationship between N, the

number of planes contributing to the x-ray reflection, and the FWHM W_L of the reflection

is:

$$N = \frac{0.89}{W_L}. \qquad (3.4)$$

The unequal distribution of the magnitude of the rotation angles, giving rise to the

L=1 reflection, has a coherence length therefore of 6.9 perovskite unit cells, or 1.15

superlattice unit cells. The alternating vertical pattern of the octahedral rotation,

producing the L=3/2 reflection, has a similarly short coherence length. In comparison, the

in-plane (h and k) widths of these reflections are at most 0.01 – indicating an in-plane

coherence length of approximately 80 perovskite unit cells – and the superlattice

structural reflections, as in Figure 3.5 (a), are even narrower. With a FWHM W_L=0.003

for the (0 0 2) reflection associated with the atomic layering, Eq. (3.4) puts the number

of planes contributing to the (0 0 2) reflection at 293, amounting to approximately half of

the 200 nm total thickness of the heterostructure. The short octahedral coherence length is

consistent with our expectation that, because of the small octahedral rotation between

BaO layers, the coupling of the octahedral rotations across the $BaTiO_3$ component layers

will be weak and that the pattern of alternating rotations in the vertical direction can thus

be broken at the BaO layers at minimal energetic cost. The oxygen octahedral rotation

pattern can thus be pinned locally by static structural disorder, effectively randomizing

the rotational configuration at large distances and leading to the short coherence lengths

observed here.

3.6 Response to Applied Electric Fields

The time dependence of electric-field-induced changes in the structure of the

superlattice was probed using the variation of the intensities of the oxygen octahedral

x-ray reflections. There are two possible origins of variations in the intensity of x-rays

scattered to a fixed point in reciprocal space near an octahedral reflection: (i) the change

in the lattice parameter due to piezoelectricity shifting the distribution of intensity associated with the x-ray reflection and (ii) the atomic arrangement and structure factor being modified by the applied field. The piezoelectric shift in the lattice parameter is apparent in the evolution of the superlattice structural (0 0 2) reflection in Figure 3.5 (a), corresponding to a strain of 0.3%. The corresponding simultaneous shift in L for the (3/2 1/2 1) reflection is $\Delta L = -0.003$, much less than the natural width $W_L = 0.12$ of this reflection. The piezoelectric shift in the (3/2 1/2 1) thus leads to a decrease by 0.06% in the intensity at the unstrained (3/2 1/2 1) wavevector, which is much smaller than what can be expected from the change in the structure factor. The change in the octahedral structure can thus be probed by monitoring the intensity arising from the (3/2 1/2 1) reflection at a fixed point in reciprocal space.

Figure 3.5 (b) shows that during the 400 ns application of a 62.5 MV/m square pulse the intensity of the (3/2 1/2 1) reflection increases by 0.8%, with a large uncertainty. This is consistent with essentially negligible change in the octahedral rotation pattern during this short time interval. A 100 MV/m triangle pulse with a far
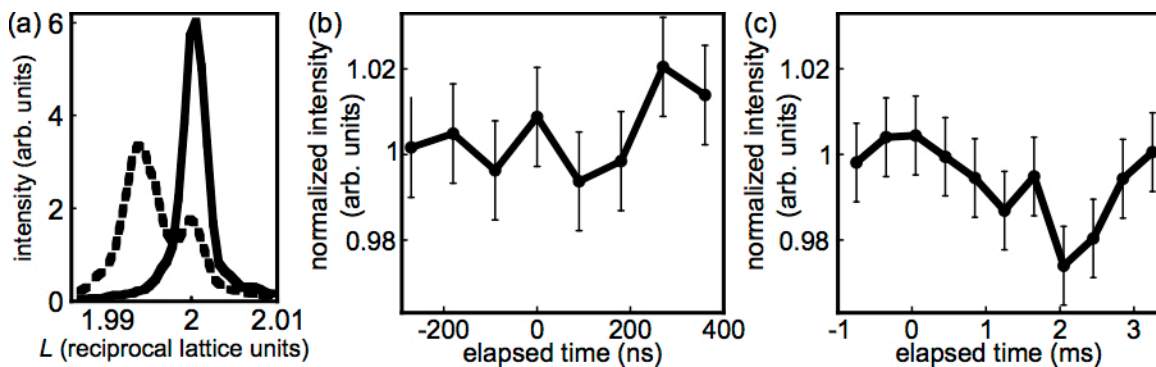
Figure 3.5 (a) Piezoelectric shift of the B2C4 (002) structural x-ray reflection at the peak field of a 2.5 ms duration, 100 MV/m electric field pulse. (b) and (c) Intensity of the B2C4 (3/2 1/2 1) reflection as a function of time during (b), a 62.5 MV/m, 400 ns square electric field pulse starting at time 0 and (c) a triangle wave with a peak electric field of 100 MV/m and a duration of 2.5 ms.

longer duration of 2.5 ms produces a decrease in the intensity by 2%, as shown in Figure

3.5 (c). The larger octahedral rotation response observed at millisecond times is

consistent with our previous observation of larger piezoelectricity at this timescale.[14]

Neither pulse duration, however, produces the large 8-16% increase in intensity predicted

in the DFT calculations. We note that the difference in the sign of the predicted and

observed changes in the intensity may be a result of the structural constraint applied

during DFT calculations that the oxygen octahedral rotations occur only around the *c*-

axis.

Based on the quantitative difference between the intensity changes observed in

Figure 3.5 (b) and (c) and the DFT predictions, we conclude that the response of the

oxygen octahedra is structurally more complicated than was assumed for the DFT

calculation. Additional measurements of the octahedral rotations and other atomic

displacements could help clarify the structural response. The DFT predictions were based

on a model in which the octahedral rotations were constrained to occur around the *c* axis,

and predicted a change in octahedral rotations largely limited to interfacial octahedra in

applied fields. We emphasize, however, that the responses of the octahedral reflections to

the applied field are time dependent, occurring over similarly long times to what has

previously been observed in the piezoelectricity of B2C4 superlattices.[14] The slow

timescale of the octahedral response is consistent with the disorder in the octahedral

rotation pattern. A long-period modulation of the octahedral rotation has also been

observed in $EuTiO_3$, with a correlation length only slightly longer than the widths we

report here for $BaTiO_3/CaTiO_3$ superlattice.[61] We thus hypothesize that disorder is at

least in part responsible for the frequency dependent dielectric properties of $EuTiO_3$, and could be equally important in other electronic materials exhibiting octahedral rotation.[62]

The connection exhibited here between the octahedral rotation geometry and the superlattice sequence suggests that superlattices can be designed with controlled disorder. The consequence of varying the disorder in this way would be that the dynamical properties could be tuned by varying the layer sequence. Potential mechanisms for varying disorder include changing the thickness of the intermediate layers in superlattices or selecting materials with specific interfacial octahedral persistence lengths. Similar considerations may apply to other systems exhibiting long-range octahedral modulations. A key feature in these systems is the existence of a multitude of disordered configurations with nearly equal energies. This diversity of configurations modifies the response of superlattices to applied fields and as a result materials exhibiting octahedral rotations share key dynamical concepts with soft condensed matter systems in which disorder is ubiquitous.[63,64]

Chapter 4: Structural Transformations in BiFeO$_3$

4.1 Introduction

BiFeO$_3$ (BFO) has several useful and interesting properties that have earned it attention recently.[19,65,66] It is both ferroelectric and antiferromagnetic, making it unusual in that it is multiferroic at room temperature.[67,68] BFO is also piezoelectric, making it useful in the creation of actuators,[69-71] sensors,[72] and nanometer-scale generators.[73-75] Moreover, unlike many commonly used piezoelectric oxide compounds, most notably PZT, a pseudo-binary solid solution of PbTiO$_3$ and PbZrO$_3$, BFO does not contain lead and therefore raises fewer health and environmental concerns.[76-78]

Previous experiments have found piezoelectric surface displacements in strained BFO films of up to 5%.[76] Beyond its practical utility, the piezoelectricity of BFO is an important property to consider when exploring its structure. The bulk BFO unit cell has a perovskite structure that is elongated along the pseudo-cubic <1 1 1> direction, giving it a rhombohedral unit cell. The central Fe^{4+} ion is displaced along this <1 1 1> direction from the center of the unit cell, giving it an electric polarization in that direction as well.

The application of an electric field can change the direction and magnitude of this displacement, drawing the Fe^{4+} (and Ba^{2+}) ions in the direction of the field, and the O^{2-} in the opposite direction, distorting the structure of the unit cell.

An electric field applied in the direction of the initial polarization draws the Fe^{4+} ions towards the Ba^{2+} ions they were already closest to, and away from the Ba^{2+} ions they were already furthest from, so the increase in the repulsive electric force between the former pairs is greater than the decrease in the repulsive electric force between the latter pairs, causing the crystal to expand in that direction. An electric field applied in a different <1 1 1> direction will cause the polarization to switch to that direction. Electric fields applied in non - <1 1 1> directions will draw the Fe^{4+} ions off of the polarization axis closest to the direction of the electric field. This would initially cause expansion in a direction close to that of the electric field, but moving the Fe^{4+} ions off of any <1 1 1> axis changes the symmetry of the crystal's unit cell, so a strong enough field could cause the structure of the unit cell to change to one that better accommodates polarization in the direction of the electric field.

Such changes in the unit cell structure are thought to be the mechanism behind the high piezoelectric response of other ferroelectric materials with similar rhombohedrally-distorted perovskite structures, such as PMN-PT.[6] While the material might be initially disordered, with different regions polarized in different <1 1 1> directions, an electric field applied in the <0 0 1> direction to the material would pole it - switching the polarization of all the domains in the material to be pointing in one of the four <1 1 1> directions with a positive out-of plane (z) component, as illustrated in
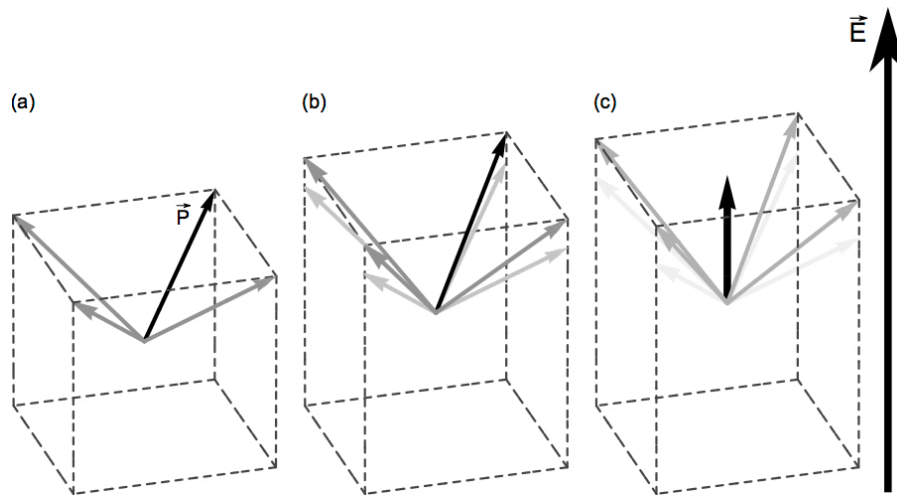
Figure 4.1 Illustration of a rhombohedral-to-tetragonal structural phase transition driven by an applied electric field. After being poled in the (0 0 1) direction, the polarization vector of a unit cell can be pointed towards one of the four upper corners of the cell, shown in (a). As an electric field is applied in the (0 0 1) direction, (b) the polarization vector rotates towards the (0 0 1) direction and the unit cell expands in that direction. (c) Eventually, the polarization vector rotates into the (0 0 1) direction, pointing towards the center of the upper plane instead of one of the four corners.

Figure 4.1(a). As the field strength increased, these four polarization vectors would all rotate towards the <0 0 1> direction, causing the crystal to expand in that direction.

At a critical field strength, all four polarization directions would switch to the <0 0 1> direction, as shown in Figure 4.1 (c), and the material would take on a tetragonal crystal structure. In this transition, the central Nb^{4+} or Mg^{4+} ion moves further in the <0 0 1> direction, becoming five-coordinated.[79] The new tetragonal structure has a larger out-of-plane lattice constant than the rhombohedral structure, causing the crystal to expand further. This additional expansion of the crystal effectively gives it an unusually high piezoelectric response.

In addition to applied electric fields, a crystal's structure can also be altered by changing its in-plan lattice parameters, which can be achieved by growing an epitaxial film of the crystal on a substrate crystal with a different in-plane structure. Changing a

crystal's in-plane lattice structure can apply compressive or tensile strain to the crystal, changing the inter-atomic distances within each unit cell. This can force the crystal to adopt a structure with lower symmetry. It can also cause the out-of-plane lattice constant to change.

In heteroepitaxial BFO films, the choice of substrate can impose in-plane compressive or tensile strain. By growing the film on a substrate material with a different in-plane lattice constant than BFO has in bulk, the in-plane lattice constant of the BFO film is constrained to match that of the substrate. A BFO film grown on LAO, such as the sample we used, is therefore under 4.4% compressive strain, as the lattice constant of LAO, 3.79 Å, is 96% of the bulk BFO pseudocubic lattice constant of 3.96 Å. A BFO film grown on a substrate with a larger or smaller lattice constant would impose less or more compressive strain, respectively.

The film lattice constant is only constrained to match that of the substrate at the interface between them, however. As the thickness of a strained film grows, the strain can relax, allowing the crystal structure of the film to become closer to the bulk crystal structure. Therefore, if the strain imposed by a particular substrate causes the film to take on a different crystal structure, a thinner film might display only the new structure, while a thicker film might also include regions of the original unstrained crystal structure, or some intermediate structure. BFO films grown on LAO take on a monoclinically distorted tetragonal-like phase (called the T phase) at small (<30 nm) thicknesses, and to include regions of mixed T and rhombohedral-like R phase as the thickness increases.[24]

Here we examine the response of the structural phases in a BFO thin film grown epitaxially on a LaAlO$_3$ (LAO) substrate. We observe reversible partial switching

between the populations of the BFO T phase and M- and T_{tilt}-phases after the application

of electric fields. We further examine the response of the film during the application of an

electric field, finding piezoelectric expansion of the T phase but not the M phase.

Moreover, we observe population shifts between the T and M phases occurring during the

application of an electric field that are of comparable magnitude to the population

changes that comprised the switching behavior previously noted.

4.2 Bulk BFO, and Strained BFO Phases

4.2.a Structure and properties

Bulk BFO is ferroelectric with a rhombohedral crystal lattice with pseudocubic

lattice parameter 3.964 Å.[80] The full rhombohedral unit cell includes two pseudocubic

unit cells, with a $\sqrt{2} \times \sqrt{2}$ expansion in-plane, and with the out-of-plane basis vector at

45° up from the plane rather than 90°, such that the angle between each pair of basis

vectors is 60°. The electric polarization is along the pseudocubic [1 1 1] direction (which

is the [0 0 1] direction of the rhombohedral unit cell).[81,82] BFO thin films grown

epitaxially on a substrate with a square in-plane crystal structure take on different

structures depending on the lattice mismatch between the BFO film and the substrate, as

well as the thickness of the film.[83-85] In thin films, the entire BFO film is strained to

match the in-plane crystal structure of the substrate, while in thicker films the strain will

start to relax towards the top of the film.

Films less than 50 nm thick under compressive strains of ~4.5%, such as those

grown epitaxially on an LAO substrate, can form a tetragonal-like monoclinic M_C T

phase, with the top face of the unit cell displaced along the [1 0 0] direction from a true
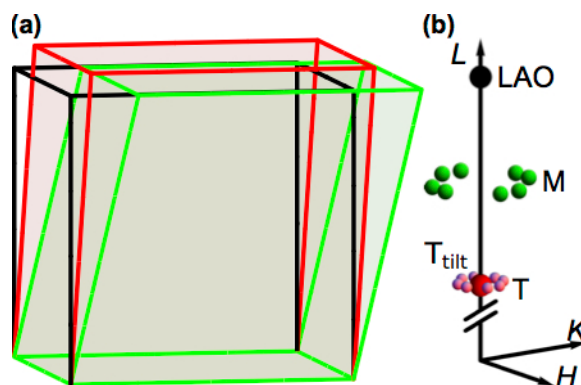
Figure 4.2 (a) T (red) and M/T_{tilt} (green) phases of BFO. The cubic structure (black) is included for comparison. (b) Model of reciprocal space near the LAO (002) reflection.

tetragonal structure.[86] Figure 4.2 (a) illustrates two different types of crystal structures present in BFO thin films grown under these conditions. Thicker films exhibit populations of this T phase, along with triclinic M and T_{tilt} phases, which have unit cells with top surfaces that are displaced along directions between [1 0 0] and [1 1 0].[87] Additional rhombohedral-like monoclinic M_A and M_B R phase and orthorhombic O phase crystal structures can be found in BFO films under tensile and smaller compressive strains.[84,88]

The [0 0 1] surfaces of the M and T_{tilt} phases are tilted with respect to the corresponding surfaces of the T phase and the LAO substrate.[87] Due to the symmetry of the LAO perovskite structure, this tilt lets the M phase and the T_{tilt} phase each take on eight different orientations, creating effectively eight M phases and eight T_{tilt} phases. These eight orientations give rise to eight different reflections distributed in a ring about the (0 0 L) axis when the film is examined with x-ray diffraction.[83] The locations of these reflections are illustrated in Figure 4.2(b), which is a diagram of the diffraction pattern produced by a BFO film grown on an LAO substrate. The T_{tilt} reflections are predicted to

be closer to the (0 0 L) axis than the M reflections, with a tilt angle of 1.5° vs. 2.7° for M

phase reflections, and to be at an l value of 1.62, compared to 1.81 for M reflections.[83]

4.2.b Morphotropic phase boundary

The different structural phases in BFO films have different directions of the

ferroelectric remnant polarization relative to the principle pseudocubic directions.[89] The

directions of the polarization vectors are illustrated in Figure 4.3. In the bulk

rhombohedral structure of BFO the remnant polarization is along the pseudocubic [1 1 1]

direction. The polarizations of the M and T_{tilt} phases likewise lie in the (1 1 0) plane,

show in green in Figure 4.3. The T phase has a polarization of approximately 60 $\mu C/cm^2$

near the [0 0 1] direction, but slightly tilted into the (0 1 0) plane, as shown in red in

Figure 4.3.[20]

Applying an electric field in the out-of-plane direction can drive the populations of

the M and T_{tilt} phases into the T phase. The polarization vector of the M phase is in the

[1 1 p] direction, with $p > 1$. An electric field along the [0 0 1] direction rotates the

direction of the polarization of this phase towards the [0 0 1], similar to the phenomenon

illustrated in Figure 4.1. The polarization vector eventually snaps into the [0 q 1]

direction, with $q < 1$, changing the structure to the nearly tetragonal monoclinic T phase,

with the monoclinic distortion in the [0 1 0] direction.

Since the T phase has a larger out-of-plane lattice constant than the M phase

(4.67 Å vs. 4.18 Å),[85] a transition from the M phase to the T phase causes the film to

expand in the out-of-plane direction. This expansion is in addition to the piezoelectric
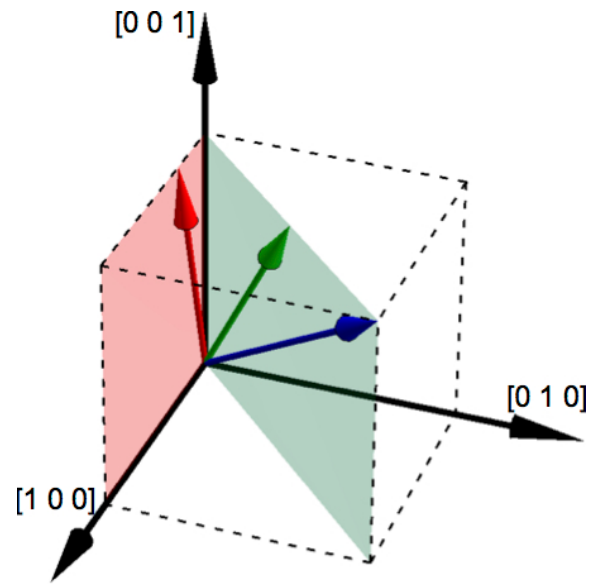
Figure 4.3 Directions of the BFO polarization vectors of the T phase (red), M phase (green), and bulk crystal (blue). The T phase vector is in the (0 1 0) plane, highlighted in pink. The bulk crystal vector is along the [1 1 1] direction. The M phase vector is in the (1 -1 0) plane, closer to the [0 0 1] direction than the bulk crystal vector.

expansion of the T phase. Films in which both phases can coexist therefore exhibit an unusually strong effective piezoelectric strain response.

Previous studies have found that the application of a strong electric field with a magnitude greater than 150 MV/m can drive a compressively strained BFO film into the T phase after a positive pulse, as observed using atomic force microscopy (AFM), piezoelectric force microscopy (PFM), and transmission electron microscopy (TEM).[9,76] The film is returned to the M phase after a negative pulse. The switching behavior is repeatable over many cycles.[9] This phase switching has been observed in these studies by making measurements before and after the application of electric fields. What is less understood is what happens to the film as the field is being applied.

Using x-ray microdiffraction we find that the application of a positive voltage pulse across the film thickness increases the population of the T phase at the expense of the M

and T_{tilt} phases, and that, conversely, the population of the T phase decreases after the application of a negative voltage pulse across the film, while the populations of the other phases increase. We also find that, in addition to the expected piezoelectric shift in the T phase (0 0 2) reflection,[90] the integrated and peak intensities of the T and M phase reflections change for the duration of the pulse, and revert back after the pulse terminates.

4.3 X-ray diffraction Studies of Electric Field-Driven Structural Transitions

A BFO thin film was grown by the research group of Prof. Long Chen at the National University of Singapore. The film was grown epitaxially to a thickness of 70 nm on a $LaAlO_3$ (LAO) substrate, with a $LaNiO_3$ (LNO) bottom electrode between the film and the substrate. Gold top electrodes 55 μm in diameter were deposited on the surface of the BFO film, forming thin-film capacitors.[85]

The static and time-resolved x-ray diffraction measurements were performed at station BL13XU of SPring-8, Harima, Japan,[91] using x-rays with a photon energy of 12.4 keV. Diffracted x-rays were detected with a gated two-dimensional pixel array detector (PILATUS 100K, Dectris). X-rays were focused onto an Au top electrode that had been contacted with a probe tip. The bottom electrode was a continuous unpatterned plane that extended to the edge of the substrate. A wire was soldered to the bottom electrode at the edge of the sample to provide an electrical contact to the bottom of the capacitor. Voltage pulses were supplied to the sample using an electronic pulse generator. Two types of volrage pulses were applied to the sample: (i) voltage pulses with a duration of 1 μs and triangular waveform and (ii) 500 ns square voltage pulses. Several magnitudes of both pulses were applied, with peak voltages up to ±15 V, corresponding to fields of 214

MV/m. The detector was synchronized to the applied voltage pulses for time-resolved measurements of the response of the BFO film to an applied electric field.[29] This experiment is described in greater detail in section 2.4.c.

Figure 4.4 is a diffraction pattern acquired from the BFO thin film under steady-state conditions. The key features visible in Figure 4.4 are the (0 0 2) reflections of the T, M and T_{tilt} phases of BFO, and the LAO substrate. The two M reflections visible in Figure 4.4 are two of the eight M reflections illustrated in Figure 4.2(b), likewise with the two T_{tilt} reflections visible adjacent to the T reflection. The arc below the T and T_{tilt} reflections is from the gold top capacitor.

The M and T_{tilt} phases each produce a ring of eight reflections around the (0 0 L) axis of the form ($\pm h \pm k\ l$) and ($\pm k \pm h\ l$), with $h > k$. Our studies included half of these – the four reflections of the form ($\pm h \pm k\ l$). The scans we performed in these studies included neither high enough nor low enough θ values to capture the ($\pm k \pm h\ l$) reflections.

4.4 Electric-Field-Driven Structural Transition

4.4.a Reversible field-induced transformation between T and M phases

4.4.a.i. Experimental Results

We explored the response of the T and M phases to the application of short-duration (1 μs) electric fields. By comparing the intensities of the reflections produced by these phases before and after applying voltage pulses across the thickness of the BFO film, we were able to observe the changes in their relative populations caused by the electric fields we applied. We applied both positive and negative voltage pulses to the film in order to determine if the phase switching we observed was reversible.
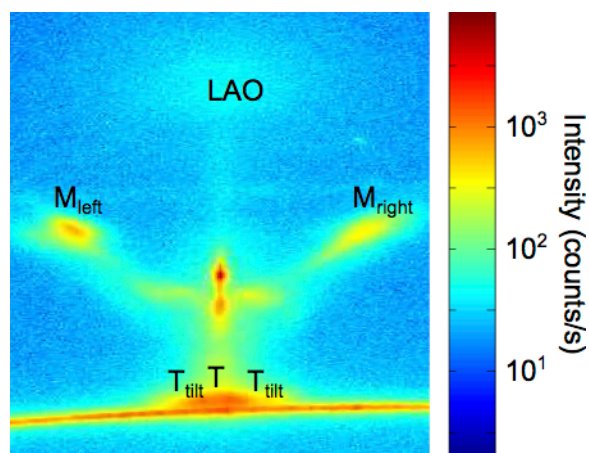
Figure 4.4 Diffraction pattern showing reflections from the different phases. Two of the M phase and T_{tilt} reflections are visible. Also visible is diffuse scattering arising from the (0 0 2) reflection of the LAO substrate. The Au (1 1 1) powder ring from the top electrode is visible just below the T and T_{tilt} reflections.

To measure the intensities of the T and M phase reflections under different conditions we performed rocking curve or θ scans, in which the sample is rotated about the in-plane axis perpendicular to the incident x-ray beam. During these scans the detector is not moved, and at each θ angle in the scan a diffraction pattern is acquired. We defined one region of interest (ROI) for the T phase reflection, two (left and right) for the M phase reflections, and another two for the T_{tilt} reflections. Since the T and T_{tilt} reflections are close to each other at similar L (and therefore θ) values, we could scan those reflections together, integrating the intensity of each reflection separately at each θ value. We also scanned the M phase reflections together, separate from the T and T_{tilt} scans.

Parts (a-c) of Figure 4.6 are plots of three rocking curve scans of the T and M phase (0 0 2) reflections. The rocking curves plotted in black in Figure 4.4 were acquired before any pulses were applied. After performing this scan, we applied a +15 V, 1 μs triangle pulse across the thickness of the film 100,000 times. The rocking curves shown

in red in Figure 4.6 were taken immediately afterwards. After these scans, we waited for 10 minutes, then applied two 1 µs, -15 V triangle pulses followed by 1000 1 µs -7 V triangle pulsed, before taking a third set of rocking curves immediately thereafter, shown in green in Figure 4.6.

After the +V pulses, the peak intensity of the T phase reflection increases by 38%, while the total integrated T phase reflection intensity increases by approximately 7%, as shown in Figure 4.6 (a). This increase in total intensity indicates a corresponding increase in the volume of the diffracting region of the film that is in the T phase, as more of the film is diffracting into the T phase reflection. This increased T phase population would have come at the expense of another phase or phases. The applied positive voltage pulses would have switched some volume of these other phases into the T phase.

The intensities of the M phase reflections decrease following the application of positive voltage pulses, as shown in Figure 4.6 (b) and (c). Just as the increase in T phase intensity indicates an increase in T phase population, so too does a decrease in M phase reflection intensity indicate a decrease in M phase population. However, this decrease in M phase population is not distributed evenly among the four M phase orientations whose reflections we scanned – the peak in Figure 4.6 (c) labeled A (M right, A) shows a much smaller decrease in intensity than the other three reflections. This variation in M phase response could be due to variations in the environment of different M phase regions. The M phase orientations are all tilted in different directions – depending on the direction of the monoclinic distortion of neighboring T phase regions some orientations may be more energetically favorable than others, making them less likely to switch into the T phase.

Negative pulses favor a transformation from the T phase to the M phase. After the negative voltage pulses, the T phase intensity drops to 15% less than its original intensity, while the M phase intensities increase. As with the response to positive voltage pulses, the change in intensity of the four M phase reflections is not uniform. The reflection labeled A in Figure 4.6 (b) (M left, A), and the reflection labeled B in Figure 4.6 (c) (M right, B) do not recover all of the intensity they lost in response to the positive voltage pulses, while the reflection labeled A in Figure 4.6 (c) recovers more than it had lost.

Figure 4.5 (d) shows the changes in the normalized peak intensity of the T phase reflection and two of the M phase reflections after the application of a sequence of positive and negative voltage pulses. Each point on the graph is derived from a rocking curve taken immediately after the application of 1000 1 μs triangular pulses of the voltage given. For the M phase reflections, the notations 'left' and 'right' refer to the regions labeled M_{left} and M_{right} in Figure 4.4, which also correspond to the two ROIs used for the M phase reflections, while 'A' and 'B' refer to the labeled intensity peaks in Figure 4.6 (b,c). With each scan, the maximum integrated intensity values for the T or M phase ROIs was extracted. Because the maximum T phase intensity is two orders of magnitude greater than the maximum M phase intensity, as shown in Figure 4.6 (a-c), these peak values were normalized by the maximum integrated intensity values of the scans taken before the application of any voltage pulses, in order better show the changes in the M phase reflections.

The intensity of the T phase reflection increases after positive pulses, and decreases after negative pulses. The intensity of the M phase reflections shows the opposite trend, decreasing intensity after positive pulses and increasing after negative pulses. Taken together, these two patterns indicate that positive voltage pulses switch some of the M phase population into the T phase, while negative voltage pulses switch some of the T phase population into the M phase. The history-dependence of the population of these different phases is also apparent in Figure 4.6(d). The M (left, B)
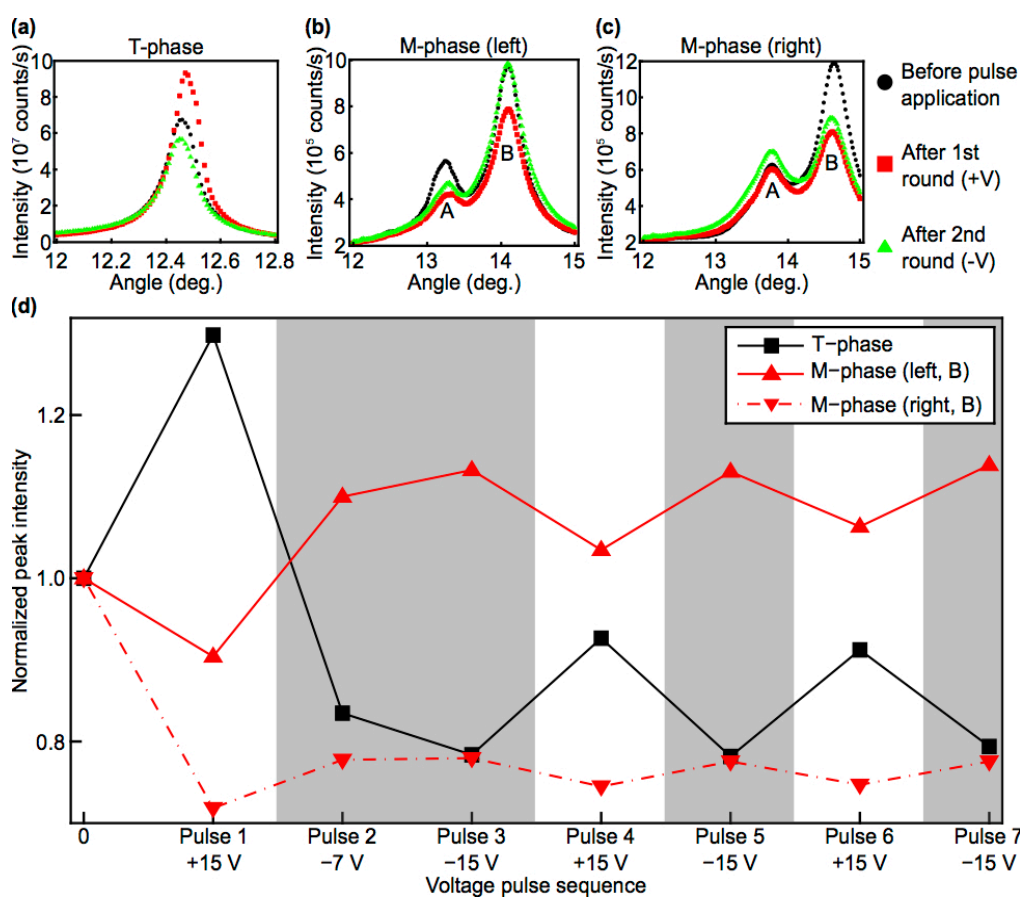
Figure 4.5 (a-c) Rocking curves of the T-phase and M-phase (002) reflections taken before the application of any electric field (black), after applying +15 V (red), and after subsequently applying −7 V (green) across the film. (d) Change in T and M phase peak intensities as positive and negative pulses are applied. The intensity of the T phase reflection increases after the application of positive voltage pulses (unshaded) and decreases after negative pulses (shaded), while the M phase intensities show the opposite trends.

reflection shows a lasting increase in intensity, while the T and M (right, B) phases do not recover the intensity they lose in their first decrease in intensity.

4.4.b.i Analysis

The diffraction studies following voltage pulses show switching behavior similar to what has been previously observed in AFM studies.[9] These studies have found the application of a large (+15 V) positive probe bias to bring a region of BFO film with T and M phase populations entirely into the T phase, while applying a negative bias recovers some of the M phase population.[19] Similarly, we find here that application of a positive voltage to the top of the BFO film we examined decreases the M phase population of the film and increases the T phase population, with +15 V increasing the T phase population by approximately 7%, and decreasing the M phase population by approximately 10%. Application of a negative voltage likewise produces a reverse effect – with the M phase population increasing and the T phase population decreasing.

There are, however, some key differences between our x-ray diffraction measurements and previous studies. The AFM studies show a complete switching into the T phase after the application of a positive voltage. Our diffraction studies, in contrast, show an incomplete the transformation between T and M phases, as there is intensity from each observed phase present after each voltage pulse. In fact, approximately 90% of the intensity of the four M phase reflections we observed remains after the application of fields of over 200 MV/m in 1 μs pulses.

A second key observation derived from the x-ray diffraction measurements is that the intensity in the M phase reflections is redistributed after the application of positive

and negative voltages. The overall M phase population increases after -V pulses and decreases after +V pulses and the populations of the eight individual M phases are also redistributed.

This redistribution of M phase reflection intensities can arise from several mechanisms which may favor some M phase orientations over others. The initial application of a positive pulse could switch isolated M phase domains to T phase, and the subsequent application of a negative pulse might switch those areas back to different M phases depending on their particular local environment. With the entire original M phase domain gone, there might not be any impetus to return to that particular orientation.

A second contribution to the redistribution among different M phase orientations is that negative voltage pulses switch entirely different T phase areas to M phase. This process would be unconnected to the distribution of M phase orientations elsewhere in the film, and would proceed entirely based on the constraints imposed by its local environment. Both phenomena would lead to redistribution of population between M phases.

4.4.b Transient response during applied electric fields

The previous section explored the steady state response of the BFO film to applied electric fields. It did not, however, examine the response of the film while the field is being applied. In this section we explore the changes the film undergoes during the application of an electric field. We observe the piezoelectric expansion of the T phase, and short-lived phase switching during each pulse. By varying the amount of time by which the application of the electric field precedes the x-ray burst used to make the

exposure, we also observe the change in M phase intensity over time as an electric field is initially applied.

4.4.b.i Field on/off comparison measurements

The response of the BFO film during the application of electric fields was characterized in two ways – a comparison of T and M phase reflection intensities while the field was on (being applied) and while it was off, and a measurement of the change in the intensity of one of the M phase reflections over time as the electric field was being applied. The first study allowed us to observe the changes to the M and T phases caused by the application of electric fields of different magnitudes. It let us differentiate the responses of the different M phase orientations, and to separate the piezoelectric response of the T phase from any changes in T phase reflection intensity. The second study allowed us to observe the transition caused by the application of the electric field as it was taking place, to determine how long it takes the film to respond.
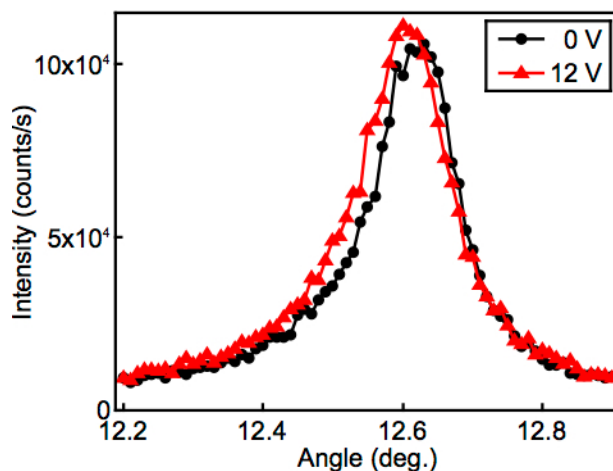
Figure 4.6 Rocking curve scans of the T phase (0 0 2) reflection taken before (black) and during (red) the application of 12 V pulses.

For the first study, the intensities of the T and M phase reflections were measured before and during the application of electric fields. The applied electric field leads to a transient expansion of the lattice due to piezoelectricity. Figure 4.6 shows rocking curves of the T phase (0 0 2) reflection taken before and during the application of 500 ns, 12 V square pulses. The same T phase ROI was used for all measurements. The peak shifts to a lower angle, indicating a piezoelectric lattice expansion of 0.15%. This shift corresponds to a converse piezoelectric coefficient d_{33} of 8.8 pm/V, less than a third of the expected value of 30 pm/V.[19] The piezoelectric expansion disappears when the field is removed after each pulse.

Additionally, the peak intensity increases by approximately 5%, and the width increases by approximately 10%. Both expansions indicate that more of the film is producing a reflection in this region of reciprocal space. These changes amount to an approximately 16% increase in the T phase population during the electric field pulse.

There is also a transient contribution to the phase transformation behavior that disappears after each pulse. This effect is apparent in measurements of the intensities of
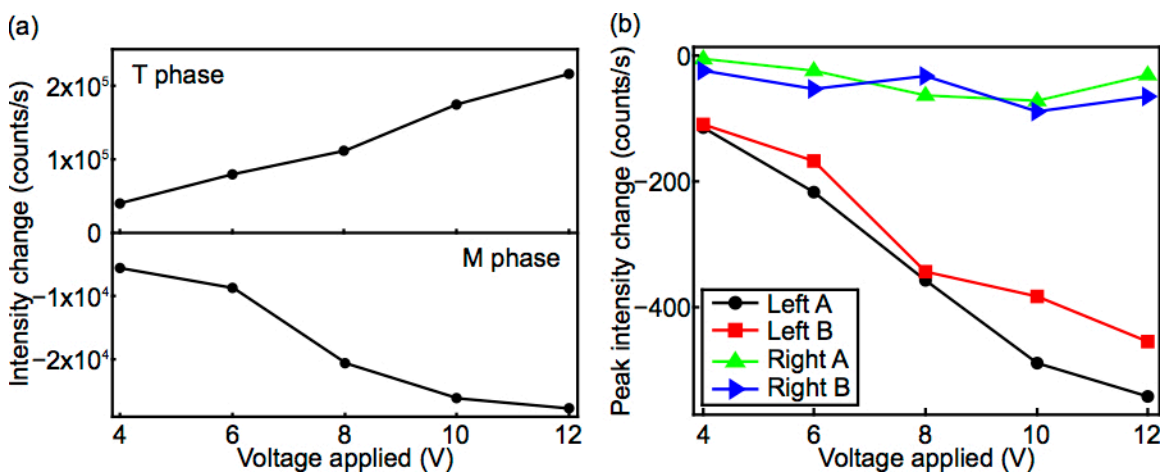
Figure 4.7 (a) Changes of the integrated intensities of the T and M phase (0 0 2) reflections during the application of different voltages. (b) Changes in peak intensities of the four individual M-phase reflections observed.

x-ray reflections from the T and M phases during applied fields. Note that in these studies the sign of the field is always in the same direction. The experiments are thus sensitive only to the transient changes during the applied field.

Figure 4.7(a) shows the changes in integrated intensity for the T and M phases before and during the application of voltage pulses of different magnitudes. The increase in T phase population from Figure 4.6 is also visible here. The 12 V data point for the T phase reflection is equivalent to the difference between the intensities, integrated over the entire rocking curve, of the 0V and 12 V curves in Figure 4.6. The value shown in Figure 4.8 (a) is 2×10^5 counts/s, while, the change in integrated intensity from Figure 4.6 is twice that much, approximately 4×10^5 counts/s.

The BFO film shows a voltage-dependent response. The increase in intensity of the T phase reflection is greater during the application of higher voltages, going from +1.5% at 4 V to +7.5% at 12 V. The intensity of the M phase reflections likewise exhibits a greater decrease with increasing voltage, dropping by six times as much at 12 V as at 4 V.

Figure 4.7 (b) shows the change in peak intensities of four different M phase reflections. As in Figure 4.5 the change in intensity is not uniform across the different M phase reflections. The intensities of the M (left) reflections decreases from a peak count rate of 8×10^4 counts/s, by 500 counts/s each. The intensities of the two M (right) reflections decrease by only 50 counts/s.

The difference between the two M phases is similar to what was observed with long-duration electric field pulses in the steady-state measurements. In both Figure 4.6 (d) and in Figure 4.8 (b) the variations in intensity of the M (right) reflections are

much smaller than those for the M (left) reflections. Although the intensity of the M

(right, B) reflection shows a 25% decrease after the initial +V application in Figure 4.5

(c), the alternating measurements in Figure 4.5 (d) were made in a more comparable

situation. During the measurements in Figure 4.8, voltage pulses were being applied

continuously during both the field-on and field-off measurements. The large change in

intensity in Figure 4.6 (c) only occurs during the first voltage pulse application, and is not

indicative of the long term behavior of the M (right) reflections.

4.4.b.ii Dynamics of M-phase response to applied electric fields

In order to learn about the timescale of the response of the BFO film to applied

electric fields, we observed the behavior of the M (left, B) reflection at different times

relative to the application of a voltage pulse. We used a series of diffraction

measurements to study the time interval required for the transformation between M and T

phases. In these studies, the intensity of the M phase reflections was measured as a

function of the delay between the application of a voltage pulse and the arrival of an x-

ray pulse. Figure 4.8 (a) shows the change in intensity of the M (left, B) reflection during

voltage pulses with magnitudes of 4 V and 12 V. The 4 V pulse causes a drop in intensity

of approximately 4% over the course of 100 ns, while the 12 V pulse causes a drop of

20% over 150 ns.

The magnitude of the intensity change is approximately 5 times greater during the

12 V pulse than it is during the 4 V pulse. The larger change induced by voltage pulses

with higher magnitudes is in agreement with the measurements shown Figure 4.7. In

Figure 4.8 (a) the M phase intensity drops by 5000 counts/s during the 4 V pulses, and by

30,000 counts/s during the 12 V pulses. Likewise, in Figure 4.8 (b) the M (left) reflections show a decrease in intensity of 100 counts/s for 4 V and 500 counts/s for 12 V.

Although the magnitude of the intensity change for 12 V pulses is five times greater than the change caused by 4 V pulses, the change seems to take place over similar lengths of time. Because a stronger field would both exert a stronger force on the film and ultimately cause a larger change, the response time would not necessarily be expected to depend on field strength. To make a more precise comparison, we fit the intensity vs. elapsed time data to an error function for each voltage, and used the widths of the fitted error functions as the response times. These times are plotted in Figure 4.8 (b). The response times do not increase continuously with increasing voltage, indicating that the electric field-induced shift in phase population takes approximately the same amount of time to complete regardless of field magnitude.

The changes in intensity of the reflections from the T and M phases observed during the application of electric fields, as shown in Figures 4.7 and 4.8, are in addition to the static changes in phase populations caused by the initial application of electric fields. Figure 4.8 (a) shows that the intensity of the M (left, B) reflection decreases by approximately 20% during the application of a 12 V pulse. Figure 4.6 (d) shows that the intensity of that same reflection changes by 10% after the application of a 15 V pulse. The intensity of this reflection therefore changes more while the field is being applied, then reverts back partially after the field stops being applied. This means that for each application of an electric field there is an initial change in T and M phase populations that
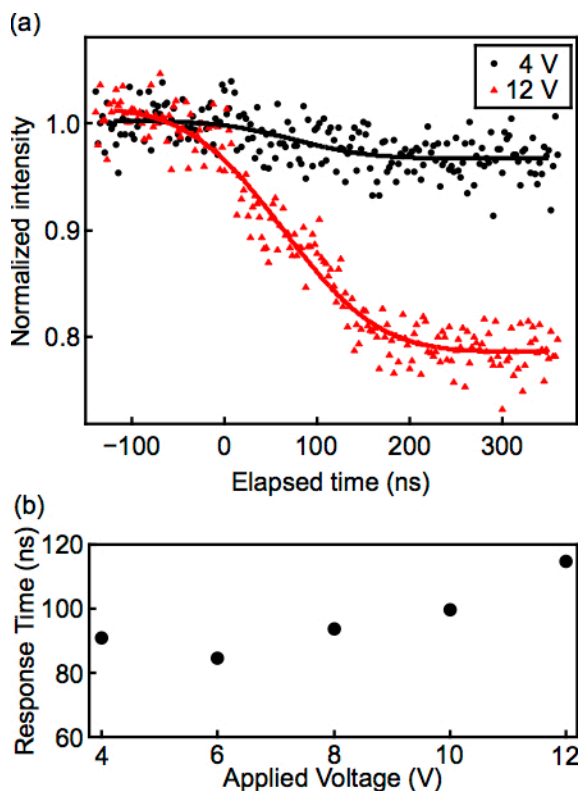
Figure 4.8 (a) Change in the intensity of the M phase (0 0 2) reflections as 4 V and 12 V pulses are applied. (b) Characteristic response times of the M (left B) reflection to the application of different voltages.

is partially reversed after the electric field is removed, in addition to reversible or

irreversible phase switching caused by the pulse.

4.5 Summary

The strained BFO thin film exhibited similar basic phase transformation behavior

observed in previous studies.[9] The key observations of the diffraction experiments,

however, build on the previous basic observations. We have found that the BFO film was

neither driven entirely into the T phase by positive voltages, nor driven entirely into the

M phases by negative voltages. In addition to this switching behavior, the BFO film

exhibited further temporary phase switching during the application of electric fields. This

additional switching during the application of an electric is of the same order of

magnitude as the long-term switching that was observed, indicating that T phase populations can readily switch back to the M phase when the electric field is removed. The characteristic response time of the phase switching showed no significant linear dependence on voltage.

Chapter 5: Conclusion

5.1 Summary of Results

5.1.a BaTiO$_3$/CaTiO$_3$ superlattices

The study of the structure and dynamics of the BTO/CTO superlattices yielded the following significant results. The study of the zero-field structure showed that the rotation of the oxygen octahedra occurred for all of the layer sequences we studied, regardless of the number of BTO or CTO units in each superlattice repeating unit. We identified the characteristic half-order reflections created by these rotations even in the superlattice film sample (B4C2) with only two consecutive CaTiO$_3$ layers. The octahedral rotation pattern in the out-of-plane direction is only coherent over the height of one superlattice repeating unit. This short coherence length indicates that the rotations are not present between even two consecutive BaTiO$_3$ layers, causing the octahedral rotations of different superlattice repeating unit layers to be decoupled. The dynamical

response of the BTO/CTO half-order reflections was only apparent in measurements with long (ms-duration) voltage pulses and could not be observed with shorter nanosecond-duration pulses.

5.1.b Strained BiFeO$_3$ thin films

Compressively strained BFO films have been found in previous studies to take on several different structural phases depending on the misfit strain between the film and the substrate.[21,24,83] Under small strains the films can be in a rhombohedral-like (R) phase similar to the bulk crystal structure, while under strains greater than -4.5% they take on a tetragonal-like (T) phase. At intermediate strains, tilted phases (M and T$_{tilt}$) that resemble the R and T phases emerge, often mixed closely with the T phase. Applied electric fields switch the M and T$_{tilt}$ phases into the T phase, and back.[19,76] We found similar but incomplete switching behavior, and further found that populations of all three of these phases remained after the application of electric fields.

Our time-resolved study of the response of the strained BFO film to applied electric fields revealed that the film exhibited additional changes while the field was being applied that did not persist after the field stopped being applied. These changes took the form a reversible change in the intensities of x-ray reflection intensities, in which the structural response of the applied field disappeared after each pulse. Larger changes were observed for electric fields with higher magnitudes. The sign of the field-induced transient changes in the intensities of the x-ray reflections from the T and M phases were consistent with what was expected from the static changes to those reflections following applied fields. The intensity of the T phase (0 0 2) reflection

increased in an applied electric field, accompanied by a decrease in the intensities of the M phase (0 0 2) reflections. Together these changes indicate a temporary structural phase transition from the M to T phase by a fraction of tens of percent of the BFO thin film during the applied electric field.

In addition to switching between structural phases with different symmetries, we also found that the populations of the eight M phase orientations were redistributed by the application of alternating positive and negative voltage pulses. Of the four M phase orientations we studied, the intensities of two of them (termed left A and right B in Figure 4.5) decreased permanently. The populations of the other two (right A and left B) either returned to their initial values when the structural switching was reversed or showed a permanent increase. The different populations of regions producing different M-phase reflections did not respond equally during the applied of electric fields. The left-A and left-B M-phase reflections showed a large change in intensity during applied fields and the right-A and right-B reflections exhibited no measurable change.

5.2 Future Directions in BaTiO$_3$/CaTiO$_3$ and BiFeO$_3$

5.2.a BaTiO$_3$/CaTiO$_3$ superlattices

With our systematic measurements of the series of BTO/CTO superlattice thin films, as illustrated in Figure 3.4, we have established that there is a relationship between the number of consecutive CTO layers and the intensities half-order reflections. In addition to the series of layer sequences we have already studied one additional sequence would be particularly interesting.

The key issue is that the half-order reflections we have studied so far all include contributions from both interfacial octahedra and octahedra between CaO layers. To further explore the relationship between the presence and magnitude of oxygen octahedral rotations in $n(BaTiO_3)/m(CaTiO_3)$ superlattices, the layer pattern of the superlattices (the n and m values), and the disorder in the rotation pattern, two additional edge cases would be particularly interesting: (i) a BnC1 and (ii) B1Cm.

Identifying and measuring the intensities of the half-order reflections that indicate the presence of octahedral rotations in a BnC1 film would give us a more direct measurement of the rotation magnitude of interfacial octahedra. As a BnC1 film would have no octahedra between two CaO layers, any intensity at the location of half-order reflections would be due only to the rotations of interfacial octahedra.

An x-ray diffraction study of a B1Cm film would let us test the connection we hypothesized between the short coherence length of the octahedral rotation pattern in the out-of-plane direction and the small rotation magnitude of oxygen octahedra between BaO layers. In a film with only one $BaTiO_3$ layer per superlattice repeating unit, there would not be a layer of un-rotated octahedra to disrupt the rotation pattern, so we would expect the out-of-plane coherence length of this pattern to be similar to its in-plane coherence length, rather than being limited to the size of the superlattice repeating unit.

We do in fact have a superlattice film with a nominal composition of $1(BaTiO_3)/5(CaTiO_3)$ that we considered using for these studies. Unfortunately, we found that the average c-axis lattice constant for this film is so close to that of the $SrTiO_3$ substrate that the film and substrate do not produce separable Bragg reflections. $SrTiO_3$ can also produce half-order reflections.[92,93] The structural reflections from $SrTiO_3$ would

likely be much narrower than the superlattice half-order reflections we observed in other films due to the greater thickness of the substrate – we would not have been able to establish the origin of any half-order reflections we found. However, changing the number m of consecutive $CaTiO_3$ layers in a B1Cm superlattice film would change the average c-axis lattice constant so that it no longer matched that of the substrate. For such a film we could distinguish between reflections from the superlattice film and reflections from the substrate, allowing us to measure the out-of-plane coherence length of its oxygen octahedral rotation pattern.

On the basis of the measurements presented in this thesis I can also present a prediction of the response of other reflections in the BTO/CTO superlattice system to applied electric fields. The (3/2 1/2 1/2) reflection would be particularly interesting. The (3/2 1/2 1) reflection, which we studied, arises due to the non-uniformity of the magnitudes of the octahedral rotations within the superlattice unit. The intensity of the (3/2 1/2 1/2) reflection, however, is an indication of the average of the magnitudes of these rotations. The change in intensity of the (3/2 1/2 1/2) reflection will therefore more directly show the overall trend in the response of the octahedral rotation magnitude. My prediction is that the rotations will decrease and that the intensity of this reflection will consequently decrease as well. The measurement of the (3/2 1/2 1/2) reflection will not be complicated by the different magnitudes of the rotations exhibited by octahedra at different locations within the BTO/CTO repeating unit.

5.2.b Strained BiFeO₃ thin films

In our measurements of the electric field response of the BFO film we studied, we observed differences among the populations of the different populations of M phase orientations. The redistribution of population among them was particularly interesting. Our explanations for these variations – that they were due to local physical constraints favoring some M phase orientations over others, or that an M phase region that was completely switched into T phase would not remember which orientation to return to when switching back – are purely speculative. Further measurements of the behavior of the different M phase orientations would clarify the origins of these variations.

We could answer the question of which M phase populations were particularly favored using a series of experiments. The role of the structural constraint imposed by the elastic environment of each crystallite of the M phase can be studied by examining the redistribution of intensity among the different orientations at many spatially separated locations using high-spatial resolution diffraction. The role of the first voltage pulse, and its irreversibility can be probed by repeatedly studying the first voltage pulse in a number of devices. Such a study could examine all eight M phase (0 0 2) reflections to determine if population is truly being redistributed among them as we have hypothesized. If that were the case the total summed intensity from the eight reflections would return to the same value after each voltage pulse. A change in the total intensity of all of the M phase reflections would indicate that a more complicated structural change is taking place.

5.3 Broader Future Directions

5.3.a Other effects of structural disorder

The key concept arising from out study of the dynamics of the structural response of the BTO/CTO superlattice system to applied electric fields was that the there was a link between disorder in the octahedral rotation pattern and the slow dynamics of the piezoelectric response. This concept can now in principle be extended from the BTO/CTO superlattice materials system to other materials that exhibit similar disorder in their octahedral rotation pattern.

Dielectric studies of europium titanate ($EuTiO_3$) have shown that this material has a frequency dependent dielectric permittivity ε' as well as structurally disordered octahedral rotations.[61,62] A systematic study of the relationship between octahedral rotation disorder in this material and its slow response to applied electric fields would be valuable as a test of the concepts we have developed in this thesis.

A second direction in testing the generality of the role of octahedral disorder in slowing the piezoelectric dynamics could include systematically studying superlattices composed of materials with different magnitudes of their octahedral rotations. A comparison of the time-dependent piezoelectric response of BTO/CTO superlattices with and without multiple $BaTiO_3$ unit cells in each repeating unit (e.g. B2C4 and B1C2) was described in section 5.2.a. Other ferroelectric/dielectric superlattice combinations, with one component having octahedral rotations in bulk and the other not, could also be used to explore the connection between octahedral rotations and slow dynamics.

5.3.b Incomplete switching and leakage current

An intriguing question arising from the study of the field-induced structural phase transition in BFO was that the switching between structural phases was incomplete. The practical maximum voltage that could be applied during these studies was limited by dielectric leakage currents. Electrical measurements during the experiment, for example, showed that due to the leakage currents a significant fraction of the voltage that was nominally applied to the sample was in fact lost to resistance in the electrodes. With applied voltages with magnitudes of 15 V, the effective voltage applied across the film after 10^4 voltage pulses decreased significantly to approximately +10 V with positive voltage pulses and -5 V with negative pulses. Moreover, applying such large voltages across the film lead to cumulative increases in the leakage current. The first +15 V pulse applied to a particular capacitor pad applied 13.3 V across the film, the 100th pulse applied 12.2 V, and the 1000th applied 10.7 V. We hypothesize that larger fields could be reached, and hence larger fractions of the BFO layer transformed to the T phase, if the dielectric leakage could be decreased. Lower dielectric leakage would allow larger voltages and would lead to reduced long-term damage.

5.3.c Deliberately favoring M sub-phases

The observation that the different variants of the M-phase within the BFO thin films transform to the T phase differently leads to the intriguing possibility that the population of M-phase variants can be used to control the transformation dynamics. By varying the epitaxial synthesis conditions, for example on a miscut substrate, it may be possible to vary the population and elastic boundary conditions on the M phase

systematically. Under such conditions it may be possible to create BFO thin films that are initially composed of more easily or less easily transformed M-phase starting materials. Structural studies of the transformation to and from the T phase could probe the relationship between the initial strain state and the fraction of the phase transformed. Similar studies after the first round of electric-field-induced phase-switching could probe the degree to which the initial conditions affect the reversibility of the transformation.

A further question regarding the distribution of M-phase populations arises if the BFO layer can be completely transformed into the T phase. Here a study of the reversibility of the transformation would address whether the distribution of M-phase variants favored by the growth condition is the same as those that grow in most rapidly in the transformation back from the T phase to the M phase. We already have shown some indication in Chapter 4 that the distribution reached after switching back from the T phased is different than the as-grown state. A systematic study as a function of the initial population would address the question of what conditions favor which M phase in the switching back from the T phase.

References

[1] B. J. Hansen, Y. Liu, R. Yang, and Z. L. Wang, *ACS Nano* **4**, 3647 (2010).

[2] R. Mallick, R. Ganguli, and M. S. Bhat, *Proc IMechE Part G: J Aerospace Engineering* **228**, 690 (2014).

[3] R. Guo, L. E. Cross, S. E. Park, B. Noheda, D. E. Cox, and G. Shirane, *Phys. Rev. Lett.* **84**, 5423 (2000).

[4] D. E. Cox, B. Noheda, G. Shirane, Y. Uesu, K. Fujishiro, and Y. Yamada, *Appl. Phys. Lett.* **79**, 400 (2001).

[5] G. A. Samara, *Phys. Rev. Lett.* **77**, 314 (1996).

[6] S. E. Park and T. R. Shrout, *J. Appl. Phys.* **82**, 1804 (1997).

[7] G. Samara, *Phys. Rev.* **151**, 378 (1966).

[8] H. Y. Hwang, S. W. Cheong, N. P. Ong, and B. Batlogg, *Phys. Rev. Lett.* **77**, 2041 (1996).

[9] J. X. Zhang, R. J. Zeches, Q. He, Y.-H. Chu, and R. Ramesh, *Nanoscale* **4**, 6196 (2012).

[10] D. G. Schlom, J. H. Haeni, J. Lettieri, C. D. Theis, W. Tian, J. C. Jiang, and X. Q. Pan, *Mater. Sci. and Eng. B: Solid State Mater. for Adv. Technol.* **87**, 282 (2001).

[11] J. B. Neaton and K. M. Rabe, *Appl. Phys. Lett.* **82**, 1586 (2003).

[12] H. N. Lee, H. M. Christen, M. F. Chisholm, C. M. Rouleau, and D. H. Loundes, *Nature* **433**, 395 (2005).

[13] J. Y. Jo, R. J. Sichel, H. N. Lee, S. M. Nakhmanson, E. M. Dufresne, and P. G. Evans, *Phys. Rev. Lett.* **104**, 207601 (2010).

[14] P. Chen, J. Y. Jo, H. N. Lee, E. M. Dufresne, S. M. Nakhmanson, and P. G. Evans, *New J. Phys.* **14**, 013034 (2012).

[15] N. A. Spaldin and M. Fiebig, *Science* **309**, 391 (2005).

[16] J. Wang, J. B. Neaton, H. Zheng, V. Nagarajan, S. B. Ogale, B. Liu, D. Viehland, V. Vaithyanathan, D. G. Schlom, U. V. Waghmere, N. A. Spaldin, K. M. Rabe, M. Wuttig, and R. Ramesh, *Science* **299**, 1719 (2003).

[17] L. W. Martin, S. P. Crane, Y.-H. Chu, M. B. Holcomb, M. Gajek, M. Huijben, C.-H. Yang, N. Balke and R. Ramesh, *J. Phys.: Condens. Matter* **20**, 434220 (2008).

[18] G. Catalan and J. F. Scott, *Adv. Mater.* **21**, 2463 (2009).

[19] J. X. Zhang, B. Xiang, Q. He, J. Seidel, R. J. Zeches, P. Yu, S. Y. Yang, C. H. Wang, Y-H. Chu, L. W. Martin, A. M. Minor, and R. Ramesh, *Nature Nanotechnol.* **6**, 98 (2011).

[20] H.-J. Liu, C.-W. Liang, W.-I. Liang, H.-J. Chen, J.-C. Yang, C.-Y. Peng, G.-F. Wang, F.-N. Chu, Y.-C. Chen, H.-Y. Lee, L. Chang, S.-J. Lin, and Y.-H. Chu, *Phys. Rev. B* **85**, 014104 (2012).

[21] H. M. Christen, J. H. Nam, H. S. Kim, A. J. Hatt, and N. A. Spaldin, *Phys. Rev. B* **83**, 144107 (2011).

[22] J. H. Lee, K. Chu, A. A. Ünal, S. Valencia, F. Kronast, S. Kowarik, J. Seidel, and C.-H. Yang, *Phys. Rev. B* **89**, 140101 (2014).

[23] P. Chen, R. J. Sichel-Tissot, J. Y. Jo, R. T. Smith, S.-H. Baek, W. Saenrang, C.-B. Eom, O. Sakata, E. M. Dufresne, and P. G. Evans, *Appl. Phys. Lett.* **100**, 062906 (2012).

[24] R. J. Zeches, M. D. Rossell, J. X. Zhang, A. J. Hatt, Q. He, C.-H. Yang, A. Kumar, C. H. Wang, A. Melville, C. Adamo, G. Sheng, Y.-H. Chu, J. F. Ihlefeld, R. Erni, C. Ederer, V. Gopalan, L. Q. Chen, D. G. Schlom, N. A. Spaldin, L. W. Martin, and R. Ramesh, *Science* **326**, 977 (2009).

[25] R. Guo, L. You, M. Motapothula, Z. Zhang, M. B. H. Breese, L. Chen, D. Wu, and J. Wang, *AIP Advances* **2**, 042104 (2012).

[26] M. Ramanathan, M. Smith, J. Grimmer, and M. Merritt, *Rev. Sci. Instrum.* **73**, 1448 (2002).

[27] J. Libera, Z. Cai, B. Lai, and S. Xu, *Rev. Sci. Instrum.* **73**, 1506 (2002).

[28] J. Als-Nielsen and D. McMorrow, *Elements of Modern X-ray Physics*, London: Wiley (2011).

[29] A. Grigoriev, D.-H. Do, P. G. Evans, B. Adams, E. Landahl, and E. M. Dufresne, *Rev. Sci. Instrum.* **78**, 023105 (2007).

[30] N. Sai, B. Meyer, and D. Vanderbilt, *Phys. Rev. Lett.* **84**, 5636 (2000),

[31] E. D. Specht, H.-M. Christen, D. P. Norton, and L. A. Boatner, *Phys. Rev. Lett.* **80**, 4317 (1998).

[32] M. P. Warusawithana, E. V. Colla, J. N. Eckstein, and M. B. Weissman, *Phys. Rev. Lett.* **90**, 036802 (2003).

[33] R. Merlin, K. Bajema, R. Clarke, F. Y. Juang, and P. K. Bhattacharya, *Phys. Rev. Lett.* **55**, 1768 (1985).

[34] B. Y. Gu, B. Z. Dong, Y. Zhang, and G. Z. Yang, *Appl. Phys. Lett.* **75**, 2175 (1999).

[35] J. Sigman, D. P. Norton, H. M. Christen, P. H. Fleming, and L. A. Boatner, *Phys. Rev. Lett.* **88,** 097601 (2002).

[36] M. Dawber, C. Lichtensteiger, M. Cantoni, M. Veithen, P. Ghosez, K. Johnston, K. M. Rabe, and J.-M. Triscone, *Phys. Rev. Lett.* **95**, 177601 (2005).

[37] E. Bousquet, M. Dawber, N. Stucki, C. Lichtensteiger, P. Hermet, S. Gariglio, J. M. Triscone, and P. Ghosez, *Nature* **452**, 732 (2008).

[38] K. F. Garrity, K. M. Rabe, and D. Vanderbilt, *Phys. Rev. Lett.* **112**, 127601 (2014).

[39] C.-J. Eklund, C. J. Fennie, and K. M. Rabe *Phys. Rev. B* **79**, 220101 (2009).

[40] J. Sinsheimer, S. J. Callori, B. Bein, Y. Benkara, J. Daley, J. Coraor, D. Su, P. W. Stephens, and M. Dawber, *Phys. Rev. Lett.* **109**, 167601 (2012).

[41] J. M. Rondinelli, S. J. May, and J. W. Freeland, *MRS Bulletin* **37**, 3 (2012).

[42] T. Araki, T. Hino, and M. Ohara, *Inst. Phys. Conf. Ser.* **61**, 012026 (2014).

[43] D. A. Tenne, H. N. Lee, R. S. Katiyar, and X. X. Xi, *J. Appl. Phys.* **105**, 054106 (2009).

[44] X. Z. Lu, X. G. Gong, H. J. Xiang, *Comp. Mater. Sci.* **91**, 310 (2014).

[45] X. Wu, K. M. Rabe, and D. Vanderbilt, *Phys. Rev. B* **83**, 020104 (2011).

[46] S. S. A. Seo and H. N. Lee, *Appl. Phys. Lett.* **94**, 232904 (2009).

[47] S. M. Nakhmanson, K. M. Rabe, and D. Vanderbilt, *Phys. Rev. B* **73**, 060101 (2006).

[48] H. Das, U. V. Waghmere, and T. Saha-Dasgupta, *J. Appl. Phys.* **109**, 066107 (2011).

[49] A. Grigoriev, D.-H. Do, D. M. Kim, C.-B. Eom, B. Adams, E. M. Dufresne, and P. G. Evans, *Phys. Rev. Lett.* **96**, 187601 (2006).

[50] L. A. Dissado and R. M. Hill, *Nature* **279**, 685 (1979).

[51] K. Bhattacharya and G. Ravichandran, *Acta Mater.* **51**, 5941 (2003).

[52] C. W. Swartz and X. Wu, *Phys. Rev. B* **85**, 54102 (2012).

[53] J. Y. Jo, R. J. Sichel, E. M. Dufresne, H. N. Lee, S. M. Nakhmanson, and P. G. Evans, *Phys. Rev. B* **82**, 174116 (2010).

[54] O. Sakata, Y. Furukawa, S. Goto, T. Mochizuki, T. Uraga, K. Takeshita, H. Ohashi, T. Ohata, T. Matsushita, S. Takahashi, H. Tajiri, T. Ishikawa, M. Nakamura, M. Ito, K. Sumitani, T. Takahashi, T. Shimura, A. Saito, and M. Takahashi, *Surf. Rev. Lett.* **10**, 543 (2003).

[55] A. Grigoriev, R. Sichel, H.-N. Lee, E. C. Landahl, B. Adams, E. M. Dufresne, and P. G. Evans, *Phys. Rev. Lett.* **100**, 027604 (2008).

[56] A. M. Glazer, *Acta Cryst.* **A31**, 756 (1975).

[57] J. M. Rondinelli and N. A. Spaldin, *Phys. Rev. B* **82**, 113402 (2010).

[58] C. L. Jia, S. B. Mi, M. Faley, U. Poppe, J. Schubert, and K. Urban, *Phys. Rev. B* **79**, 081405 (2009).

[59] X. Wu, M. Stengel, K. M. Rabe, and D. Vanderbilt, *Phys. Rev. Lett.* **101**, 087601 (2008).

[60] S. J. May, J.-W. Kim, J. M. Rondinelli, E. Karapetrova, N. A. Spaldin, A. Battacharya, and P. J. Ryan, *Phys. Rev. B* **82**, 104110 (2010).

[61] J.-W. Kim, P. Thompson, S. Brown, P. S. Normile, J. A. Schlueter, A. Shkabko, A. Weidenkaff, and P. J. Ryan, Phys. Rev. Lett. **110**, 027201 (2013).

[62] V. Goian, S. Kamba, O. Pacherova, J. Drahokoupil, L. Palatinus, M. Dusek, J. Rohlicek, M. Savinov, F. Laufek, W. Scranz, A. Fuith, M. Kachlik, K. Maca, A. Shkabko, L. Sagarna, A. Weidenkaff, and A. A. Belik, *Phys. Rev. B* **86**, 054112 (2012).

[63] V. V. Daniel, *Dielectric Relaxation*, New York: Academic Press (1967).

[64] H. Scher, M. F. Shlesinger, and J. T. Bendler, *Phys. Today* **44**, 26 (1991).

[65] G. Catalan and J. F. Scott, *Adv. Mater.* **21**, 2463 (2009).

[66] L. You, Z. Chen, X. Zou, H. Ding, W. Chen, L. Chen, G. Yuan, and J. Wang, *ACS Nano* **6**, 5388 (2012).

[67] W. Eerenstein and N. D. Mathur, and J. F. Scott, *Nature* **442**, 759 (2006).

[68] J. Wang, J. B. Neaton, H. Zheng, V. Nagarajan, S. B. Ogale, B. Liu, D. Viehland, V. Vaithyanathan, D. G. Schlom, U. V. Waghmere, N. A. Spaldin, K. M. Rabe, M. Wuttig, and R. Ramesh, *Science* **299**, 1719 (2003).

[69] R. Mallick, R. Ganguli, and M. S. Bhat, *P. I. Mech. Eng. G.-J. Aer.* **288**, 690 (2014).

[70] P. Muralt, M. Kohli, T. Maeder, A. Kholkin, K. Brooks, N. Setter, and R. Luthier, *Sensor Actuat. A-Phys.* **48**, 157 (1995).

[71] S. C. Masaminidis, R. B. Karabalin, I. D. Vlaminck, G. Borghs, M. R. Freeman, and M. L. Roukes, *Science* **317**, 780 (2007).

[72] T. Fujii, S. Watanabe, M. Suzuki, and T. Fujiu, *J. Vac. Sci. Technol. B* **13**, 1119 (1995).

[73] K.-I. Park, M. Lee, Y. Liu, S. Moon, G.-T. Hwang, G. Zhu, J. E. Kim, S. O. Kim, D. K. Kim, Z. L. Wang, and K. J. Lee, *Adv. Mater.* **24**, 2999 (2012).

[74] X. Chen, S. Xu, N. Yao, and Y. Shi, *Nano Lett.* **10**, 2133 (2010).

[75] Z. L. Wang and J. Song, *Science* **312**, 242 (2006).

[76] A. R. Damodaran, C. W. Liang, Q. He, C. Y. Peng, L. Chang, Y. H. Chu, and L. W. Martin, *Adv. Mater.* **23**, 3170 (2011).

[77] E. Cross, *Nature* **432**, 24 (2004).

[78] S. Yasui, O. Sakata, M. Nakajima, S. Utsugi, K. Yazawa, T. Yamada, and H. Funakubo, *Jpn. J. Appl. Phys.* **48**, 09KD06 (2009).

[79] A. J. Hatt and N. A. Spaldin, *Phys. Rev. B* **81**, 054109 (2010).

[80] F. Kubel and H. Schmid, *Acta. Cryst.* **46**, 698 (1990).

[81] D. Lebeugle, D. Colson, A. Forget, and M. Viret, *Appl. Phys. Lett.* **91**, 022907 (2007).

[82] O. Diéguez, P. Aguado- Puente, J. Junquera, and J. Íñiguez, *Phys. Rev. B* **87**, 024102 (2013).

[83] Z. Chen, S. Prosandeev, Z. L. Luo, W. Ren, Y. Qi, C. W. Huang, L. You, C. Gao, I. A. Cornev, T. Wu, J. Wang, P. Yang, T. Sritharan, L. Bellaiche, and L. Chen, *Phys. Rev. B* **84**, 094116 (2011).

[84] Z. Chen, Z. Luo, Y. Qi, P. Yang, S. Wu, C. Huang, T. Wu, J. Wang, C. Gao, T. Sritharan, and L. Chen, *Appl. Phys. Lett.* **97**, 242903 (2010).

[85] Z. Chen, Z. Luo, C. Huang, Y. Qi, P. Yang, L. You, C. Hu, T. Wu, J. Wang, C. Gao, T. Sritharan, L. Chen, *Adv. Funct. Matter.* **27**, 133 (2011).

[86] F. Pailloux, M. Couillard, S. Fusil, F. Bruno, W. Saidi, V. Garcia, C. Carrétéro, E. Jacquet, M. Bibes, A. Barthélémy, G. A. Botton, and J. Pacaud, *Phys. Rev. B* **89**, 104106 (2014).

[87] K. Ujimoto, T. Yoshimura, K. Wakazono, A. Ashida, and N. Fujimura, *Thin Solid Films* **550**, 738-741 (2014).

[88] J. H. Lee, K. Chu, A. A. Ünal, S. Valencia, F. Kronast, S. Kowarik, J. Seidel, and C.-H. Yang, *Phys. Rev. B* **89**, 140101 (2014).

[89] Z. Chen, X. Zou, W. Ren, L. You, C. Huang, Y. Yang, P. Yang, J. Wang, T. Sritharam, L. Bellaiche, and L. Chen, *Phys. Rev. B* **86**, 235125 (2012).

[90] P. Chen, R. Sichel-Tissot, J. Y. Jo, R. T. Smith, S. H. Baek, W. Saenrang, C. B. Eom, O. Sakata, E. M. Dufresne, and P. G. Evans, *Appl. Phys. Lett.* **100**, 062906 (2012).

[91] O. Sakata, Y. Furukawa, S. Goto, T. Mochizuki, T. Uraga, K. Takeshita, H. Ohashi, T. Ohata, T. Matsushita, S. Takahashi, H. Tajiri, T. Ishikawa, M. Nakamura, M. Ito, K. Sumitani, T. Takahashi, T. Shimura, A. Saito, and M. Takahashi, *Surf. Rev. Lett.* **10**, 543 (2003).

[92] S. R. Andrews, *J. Phys. C: Solid State Phys.* **19**, 3721 (1986).

[93] J. Hong and D. Vanderbilt, *Phys. Rev. B* **87**, 064104 (2013).